THE ASTROPHYSICAL JOURNAL, 000:00–00, 1999

THE DOUBLE NUCLEUS AND CENTRAL BLACK HOLE OF M 31

JOHN KORMENDY,[1]
Institute for Astronomy, University of Hawaii, 2680 Woodlawn Dr., Honolulu, HI 96822, and
Universitäts-Sternwarte, Scheinerstraße 1, Munich 81679, Germany;
kormendy@ifa.hawaii.edu

AND

RALF BENDER,[1]
Universitäts-Sternwarte, Scheinerstraße 1, Munich 81679, Germany;
bender@usm.uni-muenchen.de
Received 1998 August 6; accepted 1998, November 10

ABSTRACT

New spectroscopy of M 31 supports Tremaine's (1995, AJ, 110, 628) model that both nuclei are a single eccentric disk of stars orbiting the black hole (BH). The kinematics and *Hubble Space Telescope* photometry are used to measure the offset of the BH from the center of mass. This confirms that the BH mass is $\sim 3 \times 10^7$ $M_\odot$ by a technique that is nearly independent of stellar-dynamical models.

We present spectroscopy of the nucleus of M 31 obtained with the Canada-France-Hawaii Telescope and Subarcsecond Imaging Spectrograph. Spectra at the Ca infrared triplet lines (seeing $\sigma_* = 0\farcs27$) are used to measure the stellar kinematics and spectra at the Mg I b lines ($\sigma_* = 0\farcs31$) are used to measure metallicities. We also measure nonparametric line-of-sight velocity distributions (LOSVDs). All spectra confirm the steep rotation and velocity dispersion gradients that imply that M 31 contains a 3.3×10^7 $M_\odot$ central dark object. At $\sigma_* = 0\farcs27$, the maximum bulge-subtracted rotation velocity of the nucleus is 233 ± 4 km s^{-1} on the P2 side, and the maximum velocity dispersion is 287 ± 9 km s^{-1}. The dispersion peak is displaced by $0\farcs20 \pm 0\farcs03$ from the velocity center in the direction opposite to P1, confirming a result by Bacon *et al.* (1994, A&A, 281, 691). The higher-surface-brightness nucleus, P1, is colder than the bulge, with $\sigma \simeq 100$ km s^{-1} at $r \simeq 1''$. Cold light from P1 contributes at the velocity center; this explains part of the $\sigma(r)$ asymmetry. The nucleus is cold at $r \gtrsim 1''$ on both sides of the center.

Our results are used to test Tremaine's model that the double nucleus is a single eccentric disk of stars orbiting the BH. (1) The model predicts that the velocity center of the nucleus is displaced by $0\farcs2$ from P2 toward P1. Our observations show a displacement of $0\farcs08 \pm 0\farcs01$ before bulge subtraction and $0\farcs10 \pm 0\farcs01$ after bulge subtraction. (2) The model predicts a minimum $\sigma \simeq 135$ km s^{-1} at P1. We observe $\sigma = 123 \pm 2$ km s^{-1}. Observations (1) and (2) may be reconciled with the model if its parameters are tweaked so that the orbital eccentricity is made larger and the orientation of the orbits is made to point more nearly at us. (3) The model rotation curve is asymmetric; at perfect resolution, V is 60 km s^{-1} higher on the P2 side than on the P1 side. At $\sigma_* = 0\farcs27$, we observe an asymmetry of 54 ± 4 km s^{-1} after bulge subtraction. We regard this as confirmation of the model's essential idea that stellar orbits are eccentric and coherently aligned. (4) The model predicts that P1 and P2 should have the same stellar population. We confirm this: P1 is more similar to P2 than it is to the bulge, or to a globular cluster, or to M 32. This makes it unlikely that P1 consists of accreted stars. (5) Our observation that there is cold light on both sides of the center implies, if the nucleus is an eccentric disk, that some stars have escaped from the P1 – P2 alignment and have phase-mixed around the galaxy's center.

The dispersion peak coincides with a cluster of ultraviolet-bright stars seen in *Hubble Space Telescope* images. We propose that the BH is in this cluster. Its center is displaced by $0\farcs068 \pm 0\farcs010$ from the bulge center. If we put a 3.3×10^7 $M_\odot$ dark object in the UV cluster and adopt the dynamically determined mass-to-light ratio of the stars, then the center of mass (COM) of the bulge, nucleus, and dark object coincides with the bulge center to within $0\farcs017 \pm 0\farcs016$. The COM also agrees with the velocity center of the bulge and outer nucleus. Therefore, the asymmetry of the stars in the double nucleus supports our suggestion that the BH is in the UV cluster. If the stars have a normal mass-to-light ratio, then the location of the COM also confirms the mass of the BH, largely independent of dynamical models.

Tremaine's model implies that any dark cluster alternative to a BH is less than $0\farcs13 \pm 0\farcs03 = 0.49$ pc in radius. The observed mass-to-light ratio is $M/L_V \simeq 300$ in a cylinder of radius $r = 0\farcs13$ and $M/L_V \simeq 2200$ in a sphere of radius $r = 0\farcs13$. This is much larger than previous measurements of M/L_V. This result and the COM argument strengthen the detection of a central dark object in M 31.

[1] Visiting Astronomer, Canada–France–Hawaii Telescope, operated by the National Research Council of Canada, the Centre National de la Recherche Scientifique of France, and the University of Hawaii.

1. INTRODUCTION

M 31 is of special importance to our understanding of galaxy centers: it contains the nearest normal bulge (see Kormendy 1993), it shows strong evidence for a central BH of mass $M_\bullet \simeq 3 \times 10^7$ M$_\odot$ (Kormendy 1987, 1988a, b; Dressler & Richstone 1988; Richstone *et al.* 1990; see Kormendy & Richstone 1995 [KR95] for a review), and it contains a nucleus (Johnson 1961; Kinman 1965; Sandage 1971), i.e., a nuclear star cluster that is dynamically distinct from the bulge (Tremaine & Ostriker 1982). Nuclei are rare in bulges and elliptical galaxies (Lauer *et al.* 1995). They are poorly understood; it is not even clear that they represent only a single kind of phenomenon. The nucleus of M 31 is special in one other respect. We have known since the *Stratoscope II* observations of Light *et al.* (1974) that it is asymmetric; its axial ratio is $\simeq 0.6$, and the brightest spot is near the NE end. Then Lauer *et al.* (1993) observed it with the *Hubble Space Telescope* (*HST*) and discovered that the nucleus is double.

This was a surprising result: at the observed projected separation, $2r = 0\farcs49 = 1.7$ pc, a relative velocity of 200 km s^{-1} implies a circular orbit period of 50,000 y. If the two nuclei were compact star clusters in orbit around each other, dynamical friction should make them merge within a few orbital times. There are ways to reduce the friction: P1 may fortuitously corotate with the stars of P2 (King *et al.* 1995), or both nuclei could be dominated by BHs. It is not clear that either effect is sufficient. Understanding the double nucleus quickly became a major puzzle.

The most promising explanation (Tremaine 1995) is that both nuclei are parts of the same eccentric disk of stars. The brighter nucleus (P1) is the one that is farther from the barycenter; it results from the lingering of stars near apocenter. The fainter nucleus (P2) results from the disk's increase in density toward the center. A BH near P2 is required to make the potential almost Keplerian; then the alignment of orbits in the eccentric disk may be maintained by the disk's modest self-gravity. Tremaine showed that the main photometric and kinematic asymmetries could be explained by the above model.

Since then, a second double center has been found in the dwarf elliptical galaxy NGC 4486B (Lauer *et al.* 1996). In this case, there is no distinct nucleus; the brightness profile is steep and featureless outside $\sim 0\farcs2$. But the difficulty of understanding the double center is the same as in M 31. Moreover, with two relatively nearby cases, it becomes very difficult to invoke a fluke. And like M 31, NGC 4486B turns out to show evidence for a central dark object; it supports the idea that double nuclei are connected to the presence of a BH (Kormendy *et al.* 1997).

So the support for Tremaine's (1995) model is growing. Nevertheless, it remains unproved. Also, a more detailed study of the nearest BH nucleus seems very desireable. Such a study, and a further test of the Tremaine model, are the purposes of this paper.

Since *HST* spectroscopy of M 31 will be available soon, it is important to note the special strengths of this paper. (1) We have long-slit spectroscopy that reaches out into the bulge with signal-to-noise ratios $S/N \gtrsim 100$ Å^{-1} (Fig. 2). This means that the nuclear rotation curve can be tied to that of the bulge with confidence, so the location of the velocity zero point can be determined reliably. (2) We have much higher velocity resolution than the *HST* FOS or FOC, so we can measure velocity dispersions $\sigma < 100$ km s^{-1}, and we can see cold components in the LOSVDs. (3) We have measurements at both Mg I b and the Ca infrared triplet. The latter are well-separated lines that are insensitive to template mismatch; they are ideally suited to LOSVD measurements (Dressler 1984). The Mg I b spectra provide a check of the kinematics and allow us to measure metallicity gradients using the well-calibrated Lick/IDS system (Faber *et al.* 1985; Trager *et al.* 1998, and references therein). Therefore the CFHT and *HST* measurements have complementary strengths.

2. BRIGHTNESS PROFILES OF THE BULGE AND NUCLEUS

Before we discuss spectroscopy, we need to examine the brightness profiles of the bulge and nucleus to see how far out in radius the nucleus extends. We do this by fitting analytic functions to the bulge profile and extrapolating them to the center. Finding the best function for the bulge requires a bulge-disk decomposition. The bulge proves to have a Sérsic (1968) profile, $\ln I \propto r^{1/n}$, with $n = 2.19 \pm 0.10$.

Figure 1 shows the major-axis V-band brightness profile of M 31 from $0\farcs022$ to $5284''$. It is a composite of *HST* PC-1 data from Lauer *et al.* (1993), CFHT photometry with resolution $\sigma_* = 0\farcs16$ from Wainscoat & Kormendy (1998), and data at large radii from Hoessel & Melnick (1980) and from Walterbos & Kennicutt (1987). In the $r^{1/4}$ plot, the regions dominated by the nucleus ($r \lesssim 4''$), by the bulge ($4'' \lesssim r \lesssim 450''$), and by the disk ($450'' \lesssim r$; see also Sandage 1961) are clearly distinguished. The photometric and kinematic differences between the bulge and nucleus strongly suggest that the nucleus is a separate component with an origin different from that of the bulge.

We first fit the bulge with the analytic function used for cuspy cores by the *HST* Nuker team (Kormendy *et al.* 1994; Lauer *et al.* 1995; Byun *et al.* 1996; Faber *et al.* 1997):

$$I(r) = I_b \, 2^{\frac{\beta-\gamma}{\alpha}} \left(\frac{r}{r_b}\right)^{-\gamma} \left[1 + \left(\frac{r}{r_b}\right)^{\alpha}\right]^{\frac{\gamma-\beta}{\alpha}}. \qquad (1)$$

Here r_b and I_b replace the former parameters core radius r_c and central surface brightness I_0: r_b is the radius at which the steep outer $I \propto r^{-\beta}$ profile breaks into the shallow inner $I \propto r^{-\gamma}$ profile, and I_b is the surface brightness at r_b. The sharpness of the break is measured by α. We fit the composite profile at $5\farcs5 \leq r \leq 300''$ where the bulge dominates (dotted lines in Fig. 1). The parameters are $\mu_b \equiv -2.5 \log I_b + \mathrm{constant} = 17.55 \pm 0.66$ V mag arcsec^{-2}; $r_b = 67\farcs7 \pm 62\farcs1$; $\alpha = 1.08 \pm 0.59$; $\beta = 1.51 \pm 0.57$; and $\gamma = 0.25 \pm 0.25$. Note that r_b is huge. It is inconsistent with the correlations between r_b and other parameters that are observed in galaxies with cuspy cores (Faber *et al.* 1997). Also, the estimated errors in several parameters are as large as their values; this is due to strong parameter coupling. We believe that the fit is operationally correct in that it describes the profile between $5\farcs5$ and $300''$ but physically meaningless because r_b is controlled by the gentle curvature of the overall bulge profile and not by a true core. Furthermore, the extrapolation to $r = 0$ is implausible. There is an even bigger problem when we decompose the profile between $5\farcs5$ and $5000''$ into the sum of Equation (1) and an exponential disk: the inner slope, $\gamma = 0.23 \pm 0.33$, is indeterminate. This means that we are using the wrong fitting function. In particular, and contrary to the conclusions expressed in previous papers (e. g., Kormendy 1985), it means that there is no evidence that the bulge of M 31 has a core. A consequence is that M 31 is no longer inconsistent with the core fundamental plane correlations.

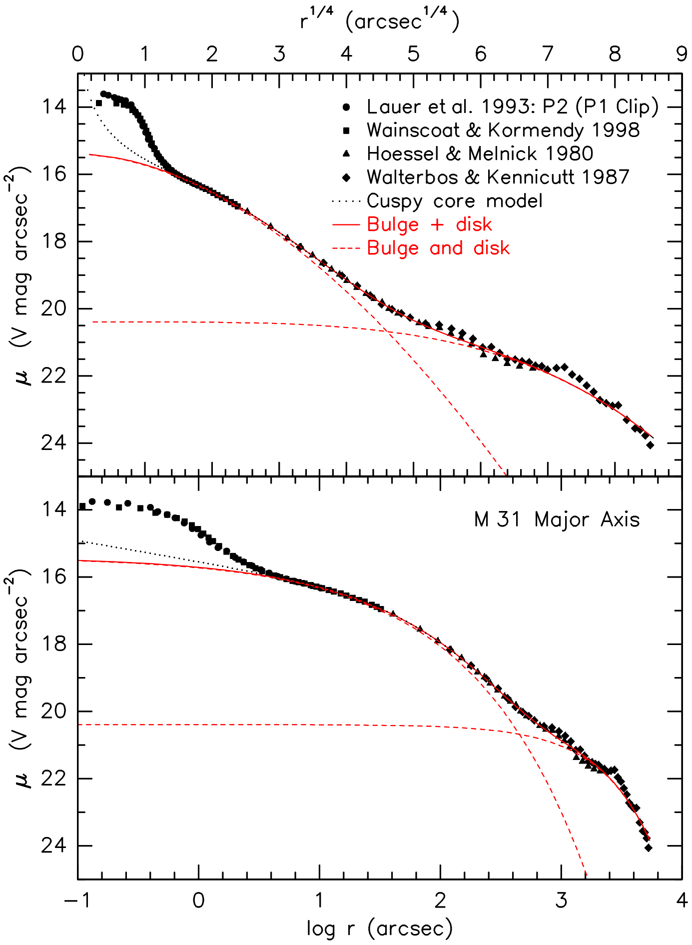

FIG. 1. Major-axis V-band surface brightness profile of M 31 plotted against $r^{1/4}$ (top) and log r (bottom). The G-band data of Hoessel & Melnick (1980) have been converted to V using the $G - R$ color profile (see their § 2; radii have been multiplied by 1.035 as suggested by Walterbos & Kennicutt 1987). The *HST* points (Lauer *et al.* 1993) are the profile of the central nucleus (P2) in the side away from P1; therefore they include as little light from P1 as possible. The total profile of P1 and P2 is asymmetrical but brighter than the filled circles show, so the nucleus is even more distinct from the bulge than the figure suggests. The dotted line shows the fit of the cuspy core profile, Equation (1), between 5.″5 and 300″. The solid line shows the adopted decomposition, a fit between 5.″5 and 5300″ of an $r^{1/n}$ bulge plus an exponential disk (Equation 2).

More meaningful results are obtained by making a bulge-disk decomposition (Kormendy 1977) using a fitting function for the bulge that is suitable for the main body of an elliptical galaxy. However, it is clear from the top panel of Fig. 1 that the bulge of M 31 is not a de Vaucouleurs (1948) $r^{1/4}$ law. We tried a decomposition into two exponentials (Andredakis & Sanders 1994); it did not work. This is not a surprise, because exponentials are characteristic of pseudobulges in late-type galaxies, i.e., high-density central regions that contain large amounts of Population I material and that probably formed out of disk gas transported inward by nonaxisymmetries in the gravitational potential (Kormendy 1993). Instead, the bulge of M 31 is well fitted by a Sérsic (1968) $r^{1/n}$ law with $n < 4$.

We therefore made a nonlinear least-squares fit of an $r^{1/n}$ law plus an exponential,

$$I(r) = I_{\mathrm{bulge},0}\; e^{-(r/r_n)^{1/n}} + I_{\mathrm{disk},0}\; e^{-r/r_1}\ , \qquad (2)$$

to the photometry in Figure 1 at $r \geq 5.''5$. The five parameters are strongly coupled, so there are two problems: (i) we need to make sure that we find the deepest of what may be several χ^2 minima in diagonal valleys in parameter space, and (ii) we need to base the error estimate on the width and separation of all appropriately low minima and not just the width of the lowest minimum. A suitable algorithm has been developed by Bender (1998). Problem (i) is solved by searching a large number of points in the range allowed by the user for each parameter. The random walk is instructed to try to reduce χ^2, but the penalty for uphill steps is small enough so that all but the highest-χ^2 parts of parameter space are explored. Problem (ii) is solved by including in the error estimates the sizes and separations of all χ^2 minima that are lower than the lowest χ^2 value times $(1 + \sqrt{2N})$, N = number of degrees of freedom. These error estimates are up to a factor of 3 larger than traditional errors calculated by fitting a five-dimensional parabola to the lowest part of the χ^2 surface and asking where, for each parameter, χ^2 has increased by a factor of $(1 + \sqrt{2N})$. The above algorithm was used for all profile fits discussed in this section.

The decomposition is shown in Fig. 1. The extrapolated central surface brightness of the bulge is 15.40 ± 0.07 V mag arcsec^{-2}, $r_n = 14.''0 \pm 1.''9$, and $n = 2.19 \pm 0.10$. For the mean profile, the effective radius is $r_e = 268'' \pm 43''$ or 1.0 ± 0.2 kpc. This implies that the total bulge magnitude $m_{B,\,\mathrm{tot}} = 4.59 \pm 0.10$, corresponding to an absolute magnitude of $M_{B,\,\mathrm{tot}} \simeq -20.1$. Then the parameters of the M 31 bulge are comfortably consistent with the $n - r_e$ correlation found by Caon, Capaccioli, & D'Onofrio (1993) and with the $n - M_{B,\,\mathrm{tot}}$ correlation found by Jerjen & Binggeli (1997). The individual components and their sum are plotted in Fig. 1. The $r^{1/2.19}$ profile gives a very reasonable description of the bulge; we will use its extrapolation to $r < 5.''5$ as our estimate of the bulge light along the line of sight to the nucleus.

Then the (bulge-subtracted) magnitude of the nucleus is $V_{\mathrm{nuc}} = 12.55 \pm 0.04$. The error estimate does not include uncertainty in the functional form of the bulge model (Equation 2). However, even if we use Equation 1, V_{nuc} is only 0.19 mag fainter than the above value. Therefore we adopt $M_V = -12.1 \pm 0.2$. Black hole searches based on dynamical models imply that the mass-to-light ratio of the stars is $M/L_V \simeq 5.7$ (Kormendy 1988b; see also Dressler & Richstone 1988 and § 8, below). Hence the mass of the stars in the nucleus is $M_{\mathrm{nuc}} \simeq 3.5 \times 10^7$ M$_\odot$. The mass of the BH is comparable, $M_\bullet \simeq 3.3 \times 10^7$ M$_\odot$ ($M_\bullet$ and M/L_V have been corrected to the M 31 distance given below). The inner structure of the bulge must have been modified substantially by the formation of the nucleus and central black hole, if these were grown after the bulge was formed.

In the above and throughout this paper, we assume that the distance to M 31 is D = 770 kpc, based on Cepheids, red giant tip stars, red clump stars, and globular clusters (Freedman & Madore 1990; Holland 1998; Kennicutt *et al.* 1998; Stanek & Garnavich 1998). We assume that the Galactic extinction is A_V = 0.24 (Burstein & Heiles 1984; see also van den Bergh 1991).

3. SPECTROSCOPIC OBSERVATIONS AND DATA REDUCTION

The kinematic measurements were made during two observing runs with the Canada-France-Hawaii Telescope (CFHT) and the Subarcsecond Imaging Spectrograph (SIS). SIS includes a tip-tilt guider to improve the spatial resolution. Also, by offsetting the guide probe, we can center the object on the slit to one-pixel accuracy. It is important to have a reliable check of the centering of the nucleus on the slit. Therefore, an observing sequence consists of a series of direct images to center the object on the slit, an exposure with the slit in place but with no grism to check the centering, the object spectrum, another image through the slit but without the grism and one with neither slit nor grism to verify that the object is still centered, and a comparison spectrum. In Run 1, two of the spectra were taken at position angle PA = 55° and the other two weretaken at PA = 50°, mid-way between PA = 63° for the nucleus as a whole and PA = 43° for the line joining P1 and P2 (Lauer *et al.* 1993). The spectra were shifted to a common center and added for the analysis. Other parameters of the spectra are given in Table 1. The total integration time and seeing are given in Tables 2 and 3.

The seeing was measured on the bracketing direct images. The brightness profile of the galaxy is the same in these images and in the spectrum, so the PSF in the images is correct for the spectrum. The seeing is summarized in the Tables by quoting the Gaussian dispersion radius σ_* of a star profile, but a modified Moffat (1969) function was fitted to a composite profile of six stars to give the PSF used in the analysis. For the Run 1 spectra, this was

$$I_*(r_*) = \frac{1}{\left[1 + \left(\dfrac{r_*}{0\farcs39353}\right)^{2.67242}\right]^{1.52487}} . \qquad (3)$$

Atmospheric dispersion was negligible. The centering exposures were taken with an I filter and the same CCD that was used for the spectroscopy, so the effective wavelength was close to that of the Ca triplet. The mean zenith distances were 23°.8 for spectrum 69F097, 30°.2 for spectrum 69F125, 31°.2 for spectrum 70F236, and 21°.2 for spectrum 70F259.

After instrumental reduction, the spectra were corrected for geometric distortion and rewritten on a $\ln\lambda$ scale using the "longslit" package in the National Optical Astronomy Observatories' *Image Reduction and Analysis Facility* (Tody *et al.* 1986).

Spectra of MK standard stars chosen from Morgan & Keenan (1973) were observed and reduced similarly. Since their images were smaller than the slit, stars were trailed along the slit at position angles slightly different from 90°. After rectification, intensities were averaged along the slit to produce one-dimensional spectra with the proper instrumental dispersion. In the Fourier analysis, different K0 – 5 III stars gave almost identical results. The adopted star(s) (Table 1) gave marginally the best internal and external consistency.

Velocities V and velocity dispersions σ were calculated using a Fourier quotient (FQ) program (Sargent *et al.* 1977; Schechter & Gunn 1979) as discussed in Kormendy & Illingworth (1982) and in Kormendy & Richstone (1992). We also measured V, σ, the higher-order Gauss-Hermite coefficients h_3 and h_4, and nonparametric LOSVDs using the Fourier correlation quotient (FCQ) program (Bender 1990). FQ and FCQ agree well: when LOSVD wings are taken into account, the velocity differences between the programs are $\lesssim 2$ km s^{-1}. FCQ error estimates are based on Monte Carlo simulations to find out how well we recover known V, σ, h_3, and h_4 values. In each simulation, one of the above parameters was varied and the distribution of all output parameters was determined for 30 realizations of spectra with the noise characteristics of the observations.

The FQ kinematic measurements are listed in Table 2 and the FCQ results are listed in Table 3.

The Run 2 spectra were taken similarly; the position angle was PA = 55°. For comparison purposes, we also obtained two, 1200 s spectra of M 32 immediately before the M 31 spectra and with the identical instrument setup. The Run 2 spectra were taken at the Mg I b lines and are primarily used for line strength measurements. However, the kinematics were also measured. They are consistent with the Run 1 results, taking into account the worse seeing. Parameters of the Run 2 spectra are listed in Table 1, FCQ results are given in Table 3, and the line strength measurements are discussed in § 7.

TABLE 1

PARAMETERS OF SPECTRA

Parameter	Run 1	Run 2
Dates of observations	1993 Aug. 23/24 – 25/26	1995 Oct. 31/Nov. 1
Spectrograph	SIS	SIS
Spectra	69F097, 69F125, 70F236, 70F259	332563, 332567
Slit length	2′.5	2′.8
Scale along slit	0″.0864 pixel^{-1}	0″.15 pixel^{-1}
Slit width	0″.353 ± 0″.002	0″.37
Wavelength range	8025 – 9030 Å	4690 – 5500 Å
Reciprocal dispersion	0.982 Å pixel^{-1}	0.441 Å pixel^{-1}
Reciprocal dispersion	34.6 km s^{-1} pixel^{-1}	25.6 km s^{-1} pixel^{-1}
Comparison line FWHM	5.4 pixel	5.3 pixel
Instrumental velocity dispersion ...	80 km s^{-1}	62 km s^{-1}
Standard star	η Cyg	HD 64606, HR 2600
Standard star spectral type	K0 III	G8 V, K2 III

TABLE 2

FOURIER QUOTIENT KINEMATIC MEASUREMENTS

Sum of Four Spectra from Run 1
Exp. = 9600 s; $\sigma_* = 0\farcs27$

r	V	$\epsilon(V)$	σ	$\epsilon(\sigma)$
−47.15	−34.3	3.6	159.8	3.8
−44.17	−37.3	3.3	160.6	3.5
−41.91	−37.7	3.3	159.6	3.5
−39.83	−29.0	2.5	159.7	2.6
−36.72	−32.3	2.3	158.8	2.4
−34.17	−24.8	3.1	162.1	3.3
−32.44	−30.7	2.8	159.3	3.0
−30.69	−31.2	2.8	157.9	2.9
−29.01	−33.5	3.0	154.4	3.2
−26.38	−26.9	2.0	155.4	2.1
−23.47	−35.3	2.1	151.5	2.2
−21.22	−30.1	2.7	152.4	2.9
−19.44	−33.6	2.6	152.1	2.7
−17.76	−26.0	2.5	149.8	2.6
−16.04	−24.5	2.4	149.3	2.5
−14.29	−23.4	2.3	148.5	2.4
−12.14	−23.3	1.8	150.2	1.9
−9.93	−27.2	2.0	153.1	2.1
−8.45	−21.3	2.1	148.5	2.2
−6.97	−16.8	1.7	144.3	1.8
−5.23	−11.8	1.6	145.0	1.7
−3.96	−19.6	2.1	144.7	2.2
−3.29	−27.9	2.9	142.3	3.1
−2.86	−31.8	2.9	142.9	3.1
−2.42	−46.1	3.0	151.2	3.1
−2.12	−52.1	3.8	157.7	3.9
−1.87	−69.1	2.7	159.7	2.7
−1.51	−95.3	2.8	164.7	2.9
−1.26	−119.1	3.8	166.4	3.9
−1.09	−137.3	3.5	167.8	3.5
−0.96	−141.9	4.5	179.6	4.6
−0.87	−157.4	4.0	173.8	4.1
−0.79	−158.7	4.0	187.8	4.0
−0.70	−159.9	4.5	198.4	4.4
−0.61	−155.1	4.7	202.1	4.6
−0.53	−152.8	4.4	210.0	4.3
−0.44	−146.4	4.5	221.1	4.4
−0.35	−132.1	4.8	232.8	4.6
−0.27	−108.5	4.4	232.0	4.2
−0.18	−87.1	5.4	247.9	5.4
−0.09	−42.3	4.8	220.7	4.7
−0.01	−3.5	4.7	220.9	4.5
0.08	31.4	4.7	208.6	4.6
0.16	61.0	4.0	191.3	4.0
0.25	92.8	4.0	184.7	4.1
0.34	119.4	3.7	174.0	3.8

Sum of Four Spectra from Run 1
Exp. = 9600 s; $\sigma_* = 0\farcs27$

r	V	$\epsilon(V)$	σ	$\epsilon(\sigma)$
0.42	126.1	3.4	169.4	3.5
0.51	138.4	2.9	150.8	3.0
0.60	147.5	3.3	146.2	3.4
0.68	149.2	3.2	140.6	3.4
0.77	151.5	3.0	135.8	3.2
0.86	152.3	2.8	124.7	3.2
0.98	150.2	2.7	121.6	2.9
1.16	133.5	2.7	129.0	3.0
1.33	126.2	2.9	128.6	3.1
1.50	106.2	3.2	137.5	3.5
1.67	87.7	3.3	136.6	3.6
1.85	70.7	3.3	138.8	3.6
2.02	63.1	3.4	140.9	3.6
2.32	46.5	3.1	146.3	3.3
2.75	33.2	3.0	142.5	3.2
3.37	23.7	2.2	147.2	2.3
4.24	15.4	2.1	143.7	2.2
5.11	7.3	2.4	143.9	2.5
6.22	13.9	1.9	149.6	2.0
7.47	19.6	2.1	143.5	2.3
8.75	21.5	2.2	146.1	2.3
10.09	29.6	2.1	149.3	2.2
11.57	28.9	2.0	153.1	2.2
13.39	24.0	2.3	149.3	2.3
15.05	24.0	2.4	151.4	2.5
16.81	24.2	2.4	152.1	2.5
19.00	26.7	2.0	150.5	2.1
21.53	24.4	2.2	157.6	2.2
24.21	29.6	2.3	163.4	2.4
26.73	24.1	2.3	162.1	2.4
29.28	34.6	2.3	155.2	2.3
32.74	34.1	1.9	164.1	2.0
36.42	35.5	3.0	163.0	3.1

Sum of Spectra from Run 1 (−Bulge)
Exp. = 9600 s; $\sigma_* = 0\farcs27$

r	V	$\epsilon(V)$	σ	$\epsilon(\sigma)$
−3.81	−111	13	65	18
−3.29	−103	10	95	13
−2.86	−104	8	101	10
−2.43	−136	6	101	8
−2.13	−143	7	92	9
−1.95	−149	7	101	8
−1.78	−172	6	101	7
−1.61	−186	6	102	7
−1.43	−177	4	99	6
−1.26	−196	4	107	5
−1.13	−201	4	106	5
−1.05	−209	5	123	6
−0.96	−218	5	123	6
−0.87	−222	4	127	5
−0.79	−227	5	142	5
−0.70	−236	5	149	5
−0.61	−229	5	158	6
−0.53	−224	6	187	6
−0.44	−217	6	204	6
−0.35	−203	7	221	7
−0.27	−169	7	241	7
−0.18	−151	8	287	9
−0.09	−77	8	267	8
−0.01	−16	8	265	8
0.08	35	8	239	8
0.16	77	6	205	6
0.25	118	6	184	6
0.34	146	5	164	5
0.42	153	4	157	4
0.51	163	4	134	4
0.60	174	4	125	4
0.68	176	4	120	4
0.77	179	3	113	4
0.86	178	3	100	4
0.94	179	3	99	4
1.03	175	3	88	4
1.11	166	4	95	5
1.20	169	3	95	4
1.33	168	3	86	4
1.50	156	4	89	5
1.68	143	4	85	6
1.85	130	5	83	7
2.02	131	5	80	7
2.32	121	5	76	7
2.76	106	6	52	10
3.19	99	8	57	13

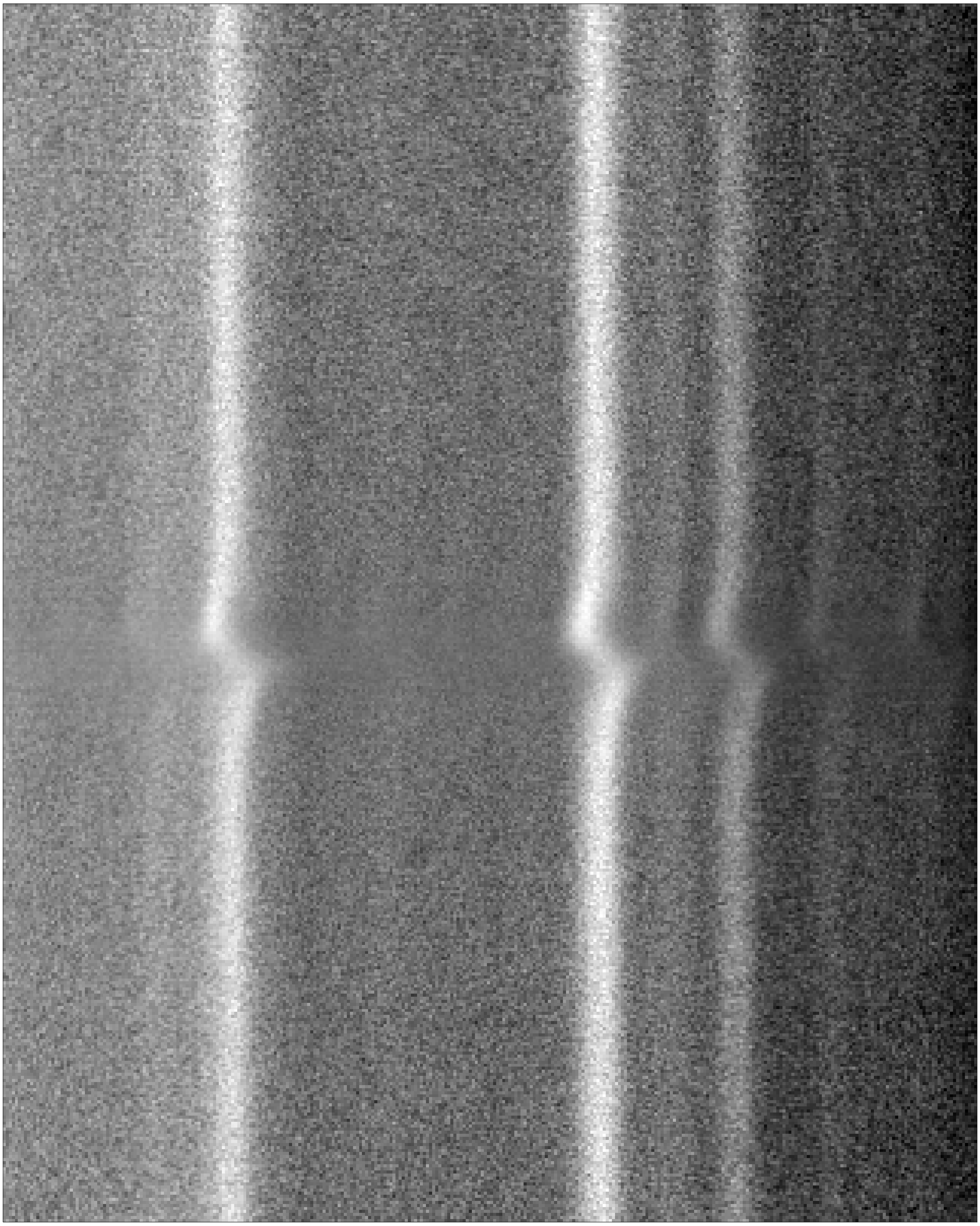

FIG. 2.– Unsharp-masked spectrum of M 31 (seeing $\sigma_* = 0\farcs27$). This is a sum of four, 2400 s exposures. The pixel size is 0.982 Å × $0\farcs0864$; the region shown is 314 Å wide by $34\farcs6$ high centered on the Ca infrared triplet. The brightness variation of the galaxy along the slit has been divided out. White corresponds to intensity 0.75 and black to intensity 1.15. The rapid rotation of the nucleus is visible as the zigzag in the spectral lines near the center. Compare Figure 1 in Kormendy (1988b), which shows a similar Mg I b spectrum at $\sigma_* = 0\farcs52$.

4. KINEMATICS

The kinematic results from the Ca infrared triplet spectra are based on the sum of four, 2400 s exposures. They are shown before and after bulge subtraction in Fig. 2 and 3, respectively. The kinematics are illustrated in Fig. 4. Here filled circles are for the spectrum as observed; it includes light from both the bulge and the nucleus. Since the bulge contributes significantly at all radii, and since it rotates slowly, it dilutes what we are trying to measure, which is the spectrum of the nucleus. The observed spectrum is analogous to a spectrum that has not been sky-subtracted. Therefore we subtracted the mean bulge spectrum at $4''.5 \leq |r| \leq 8''.0$ to remove as much as possible of the light from in front of and behind the nucleus. The mean bulge spectrum was scaled at each radius to have the brightness distribution given by Equation 2 (red solid curve in Fig. 1) after convolution with our PSF. The two-dimensional spectrum that was subtracted was also given the mean rotation curve of the bulge extrapolated inward from $r \gtrsim 5''$, i.e., $V = 2.65\,(r/1'')$ km s^{-1}. The results are robust; they do not depend strongly on the radius range in which the bulge spectrum is averaged and are insensitive to whether we subtract a spectrum with the systemic velocity or one that has the rotation curve of the bulge. The FQ reduction of the bulge-subtracted spectrum is shown by the crosses in Fig. 4. It is included in Table 2.

As in other BH galaxies, the central kinematic gradients are unresolved. The maximum apparent rotation velocity before bulge subtraction, $V = 156 \pm 2$ km s^{-1}, is reached at $0''.8$ from the center. The maximum apparent velocity dispersion is 248 ± 5 km s^{-1}. After bulge subtraction, the corresponding values are $V = 206 \pm 2$ km s^{-1} and $\sigma = 287 \pm 9$ km s^{-1}. The resolution here is essentially twice as good as that in Dressler & Richstone (1988) and in Kormendy (1988b); the bulge-subtracted maximum V and σ observed there were $V = 149 \pm 5$ km s^{-1} and $\sigma = 245 \pm 7$ km s^{-1}. Therefore the kinematic gradients get steeper as resolution improves. This is consistent with the presence of a BH. Stronger evidence for a BH is discussed in §§ 8 – 10.

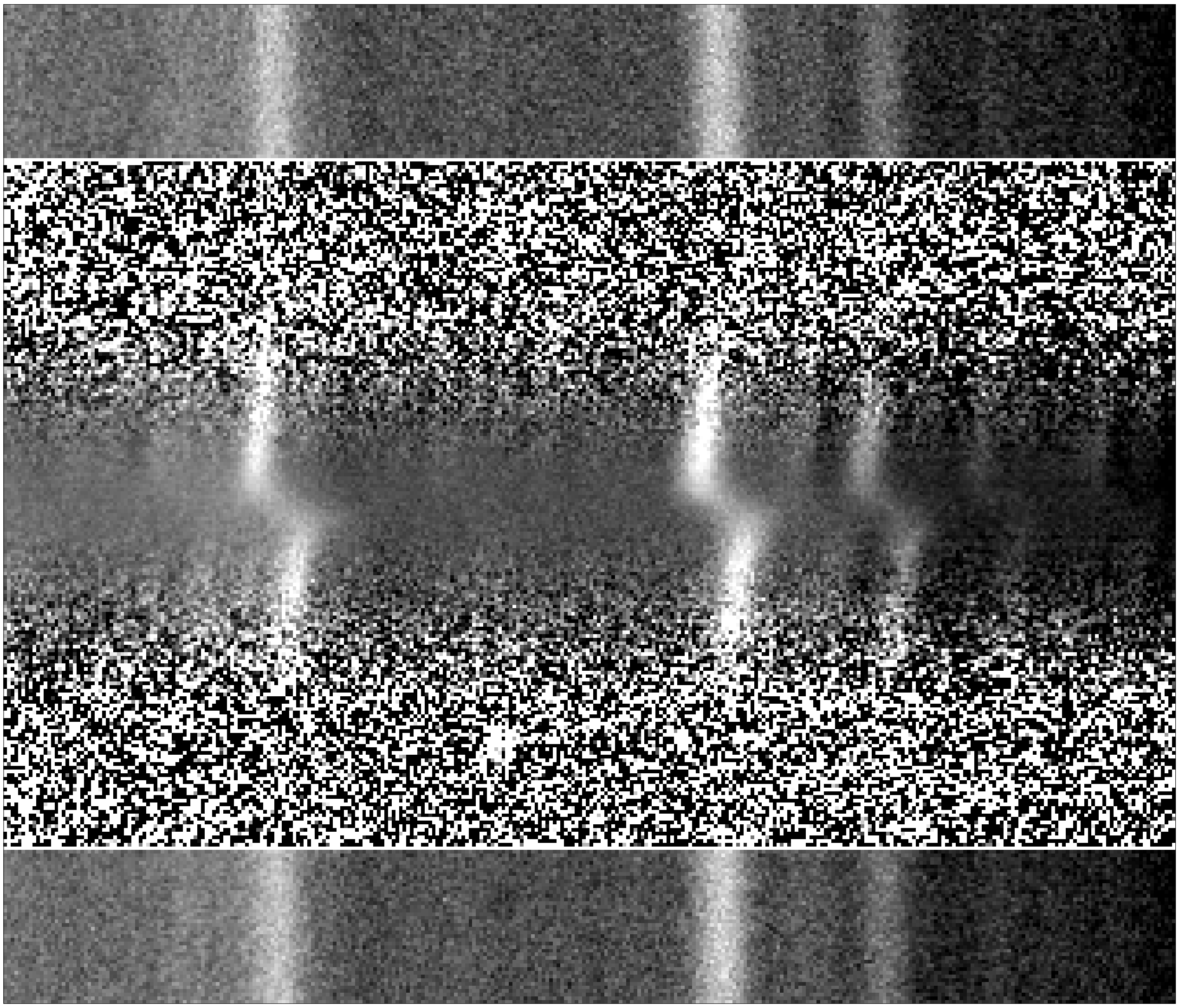

FIG. 3.– (*Center*) Unsharp-masked spectrum of M 31 after bulge subtraction. The exposure time, pixel size, wavelength region, print scale, and grayscale values are the same as in Fig. 2. The region shown is $16''.2$ high. The outermost $3''.5$ on both sides of the center are the radius range $4''.5 \leq |r| \leq 8''.0$ in which the bulge spectrum was averaged. (*Top and bottom*) These same regions on both sides of the center are shown before bulge subtraction. The bulge-subtracted spectral lines in the nucleus are clearly narrower than those in the bulge everywhere except near P2 (i. e., immediately below the center).

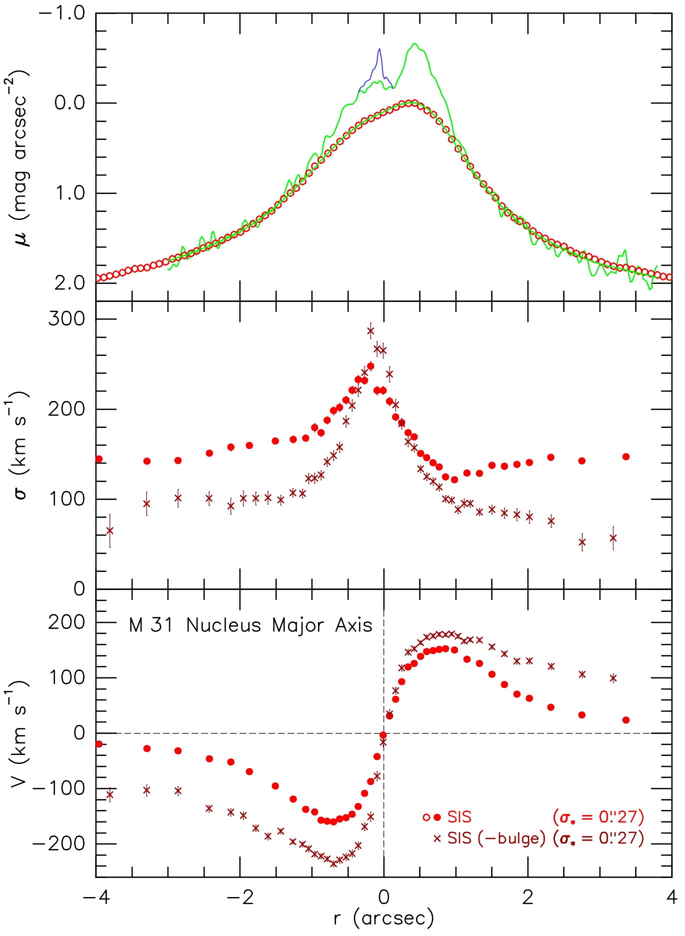

FIG. 4.– Rotation curve $V(r)$, dispersion profile $\sigma(r)$, and brightness cut $\mu(r)$ along the major axis of the nucleus of M 31. The central points of the SIS spectrum are separated by $0\farcs0864$. In the top panel, the upper green line is a $0\farcs35$-wide cut through the deconvolved I-band *HST* WFPC2 image of M 31 by Lauer *et al.* (1998); the left peak is P2; the right peak is P1. The lower green curve is a similar brightness cut through this same image after convolution with our spectral PSF (Equation 3). It agrees with the brightness cut observed in the spectrum (red circles). The blue line segment is a $0\farcs046$-wide cut through the blue cluster embedded in P2; it is taken from the V-band WFPC2 image by Lauer *et al.* (1998); see Fig. 7, below.

We confirm the conclusion of Bacon *et al.* (1994) that the velocity dispersion peak is displaced from the center of rotation in the direction opposite to P1. We observe a smaller displacement: the highest-σ point is $0\farcs18 \pm 0\farcs01$ from the velocity center, and the dispersion peak as a whole is centered $0\farcs18 - 0\farcs23$ from the velocity center. Bacon *et al.* (1994) found a displacement of $0\farcs6$. We also find a narrower dispersion peak. Both differences are due to our better resolution. Because the dispersion peak is asymmetric, smearing it moves it farther from P1.

P1 is very cold. Even in the composite spectrum, σ is smaller at $1''$ than it is in the bulge. But the bulge contributes much of the light. The bulge-subtracted spectrum is a better measure of the nucleus; it shows that $\sigma \simeq 100$ km s^{-1} at $r \simeq 1''$. It also confirms a result found by Kormendy (1988b): *the nucleus is cold on both sides of the center.* LOSVD analysis confirms both conclusions.

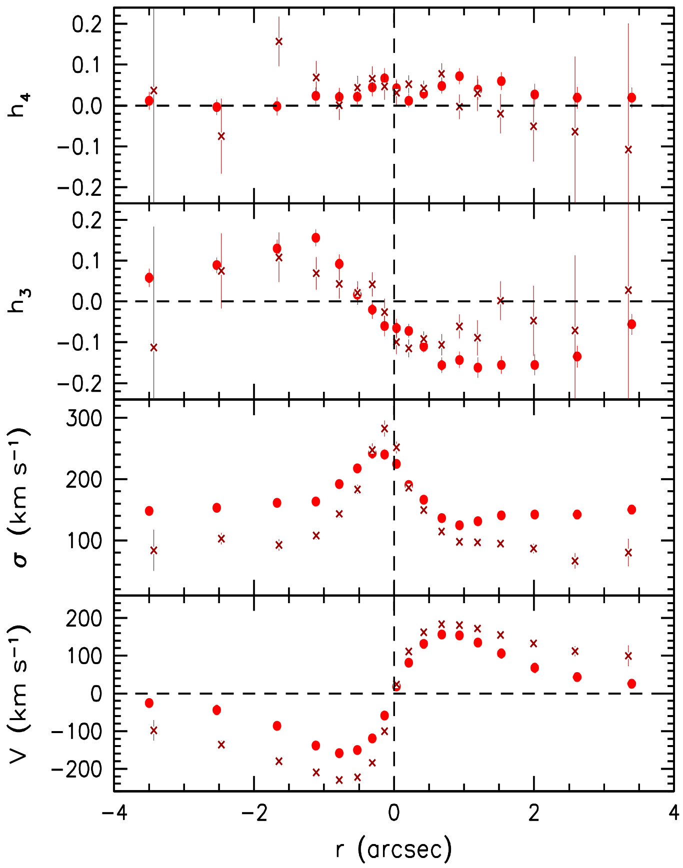

FIG. 5.– Rotation curve $V(r)$, dispersion profile $\sigma(r)$, and Gauss-Hermite parameters h_3 and h_4 of the nucleus of M 31 as derived with the FCQ program. The symbols are as in Fig. 4.

We measured non-parametric LOSVDs using the FCQ method (Bender 1990). To get higher-order information about the LOSVD shapes, we fitted them with a Gaussian plus third- and fourth-order Gauss-Hermite polynomials H_3 and H_4 (van der Marel & Franx 1993, Gerhard 1993):

$$\mathrm{LOSVD}(v) = \frac{\gamma}{\sqrt{2\pi\sigma^2}}\, e^{-\frac{(v-V)^2}{2\sigma^2}} \; .$$

$$\cdot \left[1 + h_3 H_3\left(\frac{v-V}{\sigma}\right) + h_4 H_4\left(\frac{v-V}{\sigma}\right)\right]. \quad (4)$$

The coefficients h_3 and h_4 parametrize the lowest-order asymmetric and symmetric deviations from Gaussian line profiles. Positive h_4 implies that the line profile is more triangular than Gaussian – it is more strongly peaked and has more extended wings than the best-fitting Gaussian. Negative h_4 means that the line profile is more rectangular than Gaussian. The h_4 amplitudes are generally small in ellipticals, with values less than a few percent (Bender *et al.* 1994).

Figure 5 shows the V, σ, h_3 and h_4 values for the original M 31 spectrum and for the bulge-subtracted nucleus. The corresponding LOSVDs are plotted in Figure 6. The black LOSVDs were derived from the bulge spectrum that was subtracted. Again, details of how it was constructed do not matter, because bulge rotation is negligible, and because the bulge LOSVD is almost Gaussian.

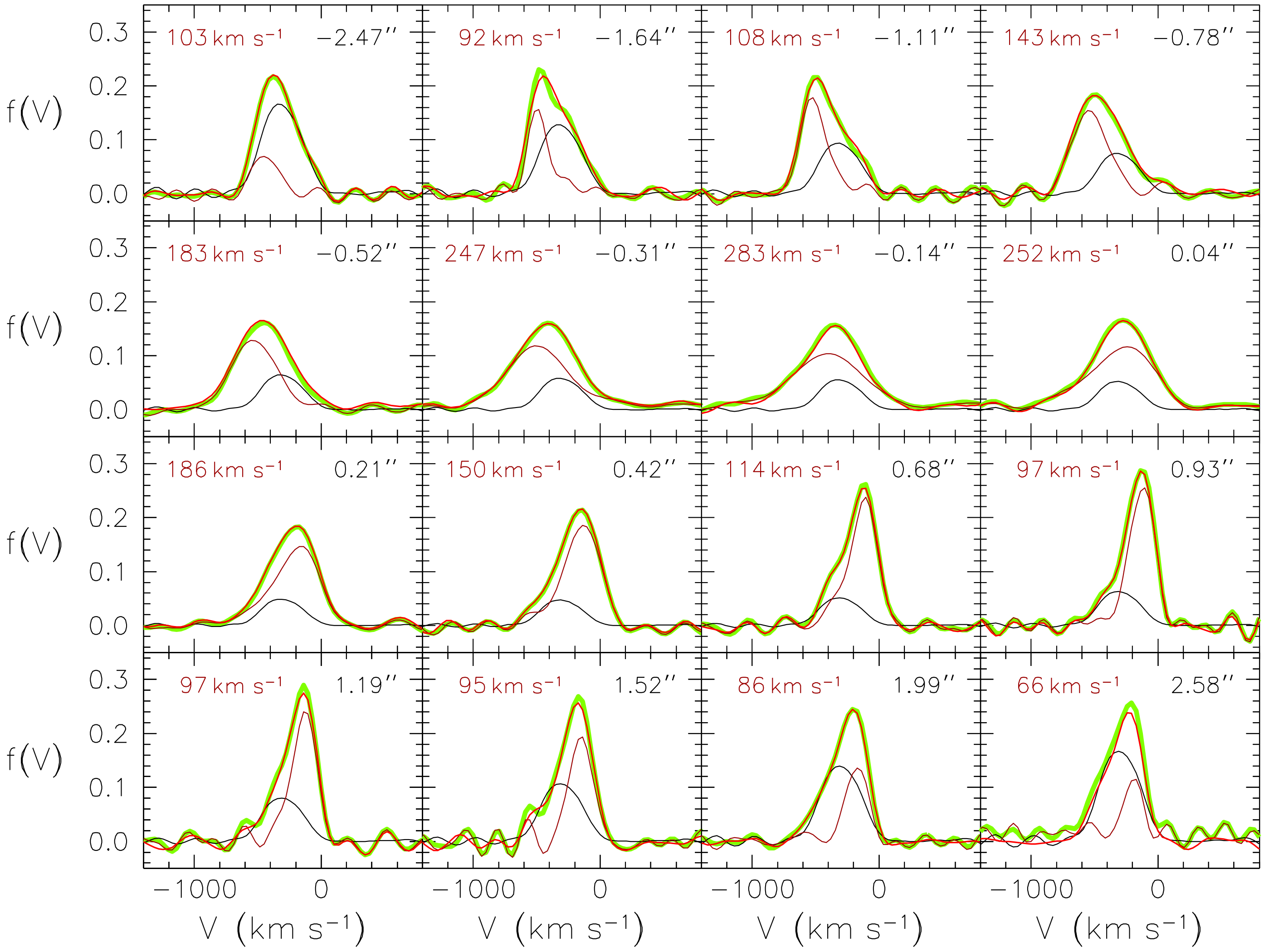

FIG. 6.– Line-of-sight velocity distributions in the same radial bins that were used to derive the kinematic results shown in Fig. 5. The black lines are for the bulge model and the brown lines are for the bulge-subtracted nucleus. The red profiles are the LOSVDs of the original spectrum, and the green lines are a reconstruction of them made by adding the bulge and nuclear LOSVDs. The radius of each bin is given at upper right in each panel, and the velocity dispersion of the bulge-subtracted nucleus is at upper left.

For checking purposes we also show in Fig. 6 the total LOSVDs reconstructed by adding the LOSVDs of bulge and nucleus weighted by their relative light contributions (Fig. 1). The original and reconstructed LOSVDs agree remarkably well.

Figures 5 and 6 show that the strong asymmetries, i.e., the large $|h_3|$ values, of the original M 31 LOSVDs are partly due to the superposition of the bulge and nucleus. But the nucleus by itself also has asymmetric LOSVDs. The h_3 amplitude correlates with V/σ as it does in other dynamically hot galaxies (Bender *et al.* 1994). However, the correlation is not perfect; $h_3(r)$ is not antisymmetric about $r = 0''$ but rather about a point slightly on the anti-P1 side of the dispersion maximum. This effect is opposite to what we would expect from PSF smearing: since P1 is brighter than P2, negative radii see more light from positive radii than vice versa, so the positive-velocity wing should be enhanced. Instead, the h_3 asymmetry may be a consequence of Tremaine's (1995) model. It predicts a sharp negative-velocity $V(r)$ maximum at $\sim 0\farcs25$ on the anti-P1 side of the dispersion peak. After PSF smearing, this would contribute negative-V wings near the dispersion peak where the mean velocity is already negative.

The LOSVDs of the nucleus have broad wings: $h_4 > 0$. Since the h_4 profile is the same at $r \lesssim 1''$ in the original and bulge-subtracted spectra, the wings are intrinsic to the nucleus. They are a natural consequence of the presence of a BH (van der Marel 1994) and a further constraint for future models of the eccentric disk.

5. *HST* WFPC2 IMAGES: REGISTRATION OF IMAGES AND SPECTRA

Interpretation of the kinematics of the nucleus requires accurate registration of the spectra with *HST* images. Lauer *et al.* (1998) have kindly provided their I-, V-, and 3000 Å-band *HST* WFPC2 images; a color composite of these is shown in Fig. 7. The I and V images were constructed from exposures dithered by 0.5 PC pixel; they have scale $0\farcs0228$ pixel^{-1}. After 40 iterations of Lucy-

TABLE 3

FOURIER CORRELATION QUOTIENT KINEMATIC MEASUREMENTS

Sum of Four Spectra from Run 1
Exp. = 9600 s; $\sigma_* = 0''.27$

r	V	$\epsilon(V)$	σ	$\epsilon(\sigma)$	h_3	$\epsilon(h_3)$	h_4	$\epsilon(h_4)$
-11.67	-24.5	3.6	157.9	3.8	0.042	0.021	-0.023	0.021
-9.97	-31.5	3.8	153.2	4.5	0.104	0.023	0.016	0.023
-7.79	-20.6	3.2	149.7	3.4	0.070	0.020	-0.028	0.020
-5.65	-14.3	2.8	150.0	3.1	0.050	0.017	-0.015	0.017
-4.36	-12.3	3.6	149.7	4.2	0.044	0.022	0.013	0.022
-3.50	-25.4	3.5	148.2	4.2	0.058	0.022	0.012	0.022
-2.53	-43.9	3.1	153.1	3.6	0.089	0.019	-0.004	0.019
-1.67	-86.4	3.9	161.2	4.4	0.130	0.022	-0.002	0.022
-1.12	-138.0	3.7	163.3	4.5	0.156	0.021	0.024	0.021
-0.78	-158.4	4.7	192.2	5.7	0.092	0.023	0.021	0.023
-0.52	-150.1	4.5	217.5	5.5	0.017	0.019	0.022	0.019
-0.31	-119.1	5.7	242.0	7.3	-0.020	0.022	0.045	0.022
-0.14	-58.5	6.5	240.1	8.6	-0.060	0.025	0.067	0.025
0.04	18.7	5.5	224.6	6.9	-0.065	0.022	0.042	0.022
0.21	81.5	3.6	190.3	4.2	-0.072	0.017	0.012	0.017
0.42	131.9	2.6	166.0	3.2	-0.110	0.015	0.029	0.015
0.68	156.5	2.9	136.3	3.7	-0.156	0.019	0.048	0.019
0.94	154.3	2.8	124.3	3.7	-0.143	0.020	0.072	0.020
1.20	134.5	3.5	131.3	4.4	-0.162	0.025	0.039	0.025
1.53	105.9	3.4	140.7	4.5	-0.155	0.022	0.060	0.022
2.01	67.8	4.1	142.3	4.9	-0.155	0.026	0.027	0.026
2.61	42.9	3.9	142.0	4.7	-0.135	0.026	0.019	0.026
3.39	26.0	4.1	150.0	4.9	-0.056	0.025	0.019	0.025
4.68	10.7	3.2	146.9	3.6	-0.010	0.020	-0.004	0.020
6.42	15.9	3.5	153.7	3.8	-0.016	0.021	-0.022	0.021
8.14	20.4	3.4	150.7	3.8	-0.051	0.021	-0.007	0.021
10.67	31.6	2.8	152.1	3.1	-0.055	0.017	-0.010	0.017

Sum of Four Spectra from Run 1 (−Bulge)
Exp. = 9600 s; $\sigma_* = 0''.27$

r	V	$\epsilon(V)$	σ	$\epsilon(\sigma)$	h_3	$\epsilon(h_3)$	h_4	$\epsilon(h_4)$
-4.37	-26.7	83.1	65.9	95.9	0.004	1.147	0.011	1.147
-3.43	-98.0	27.2	83.7	33.5	-0.113	0.296	0.037	0.296
-2.47	-135.7	10.3	102.5	9.3	0.075	0.092	-0.075	0.092
-1.64	-180.2	6.1	92.4	9.8	0.108	0.061	0.157	0.061
-1.11	-209.7	4.7	107.5	6.3	0.069	0.040	0.069	0.040
-0.78	-230.1	5.6	143.3	6.3	0.043	0.036	0.001	0.036
-0.52	-222.3	5.5	183.3	6.9	0.021	0.028	0.044	0.028
-0.31	-184.1	8.1	247.3	10.7	0.042	0.030	0.066	0.030
-0.14	-100.7	10.3	282.6	13.1	-0.026	0.033	0.047	0.033
0.04	23.8	8.2	251.6	10.0	-0.099	0.030	0.031	0.030
0.21	110.8	4.5	186.1	5.8	-0.115	0.022	0.052	0.022
0.42	162.1	3.1	149.6	3.8	-0.092	0.019	0.042	0.019
0.68	183.2	3.1	114.4	4.2	-0.106	0.025	0.078	0.025
0.93	181.2	3.1	97.4	3.5	-0.061	0.030	-0.003	0.030
1.19	172.3	4.5	96.5	5.4	-0.089	0.043	0.030	0.043
1.52	155.5	4.9	94.9	5.3	0.002	0.048	-0.020	0.048
1.99	132.4	8.1	86.4	7.9	-0.047	0.086	-0.051	0.086
2.58	111.8	13.4	66.4	12.5	-0.071	0.184	-0.064	0.184
3.35	99.8	27.2	80.2	21.8	0.028	0.308	-0.108	0.308
4.45	38.5	54.8	89.4	32.3	-0.312	0.558	-0.344	0.558

Richardson deconvolution (Richardson 1972; Lucy 1974), they have remarkably good resolution. The 3000 Å image was not dithered. As noted by Lauer *et al.* (1998), the two brightness peaks discovered by Lauer *et al.* (1993) are well confirmed; P1 is brighter than P2 in the optical. However, the small drop in surface brightness between P1 and P2 is mostly due to the small remnant visible in the optical of the ultraviolet (UV) brightness peak in P2 that was discovered by King, Stanford, & Crane (1995). They obtained a 1750 Å image with the *HST* FOC; at this wavelength, P2 is higher in surface brightness than P1. However, the excess flux is equivalent to one post-asymptotic-branch giant star, and King and collaborators found a number of such stars in the field (see also Fig. 7). It was therefore not clear that the UV source in P2 has anything to do with the BH. Nevertheless, King *et al.* (1995) suggested that it is due to the central radio source (Crane *et al.* 1992, 1993). The WFPC2 images now show that the UV source is resolved into a tiny cluster of stars. A two-row-wide brightness cut through this cluster is shown in Fig. 4 to illustrate its position with respect to the kinematic profiles. We will show in § 8 that the UV-bright cluster is likely to be the location of the BH, and we will discuss some consequences of this conclusion in §§ 8 and 9.

Our spectra were registered with the *HST* images as follows (Figure 4). The deconvolved *I*-band image from Lauer *et al.* (1998) was rotated to align the nucleus with our slit position angle and convolved with our spectral PSF (Equation 3). We then averaged the brightness in 15 rows, corresponding to our slit width of $0''.35$. This produced a brightness cut (lower green line in Figure 4) that could be shifted in radius until it agreed with the brightnesses in the spectrum (open circles). The good agreement of the PSF-convolved *HST* brightness cut with that in our spectrum confirms that our PSF is valid. It also registers the spectra with the *HST* images to $\pm 0''.007$.

6. TEST OF TREMAINE'S MODEL OF THE NUCLEUS

One aim of this paper is to test Tremaine's (1995) model of the nucleus of M 31. He proposed that both brightness peaks are parts of the same eccentric disk of stars; P1 results from the lingering of stars near apocenter, and P2 results from the disk's increase in density toward the center. The model depends on the presence of a BH near P2. This makes the potential almost Keplerian; then the alignment of elongated orbits can be maintained more easily by the disk's modest self-gravity. Tremaine's model is the most viable interpretation of the surprising observation that the nearest giant galaxy outside our own contains an asymmetrical nucleus with a short apparent lifetime. It was developed to explain kinematic data with resolution $\sigma_* \simeq 0''.5$. The present resolution, $\sigma_* \simeq 0''.27$ is about a factor of two better, and our signal-to-noise ratios are better as well. Therefore we can make an incisive test of the predictions made by the model.

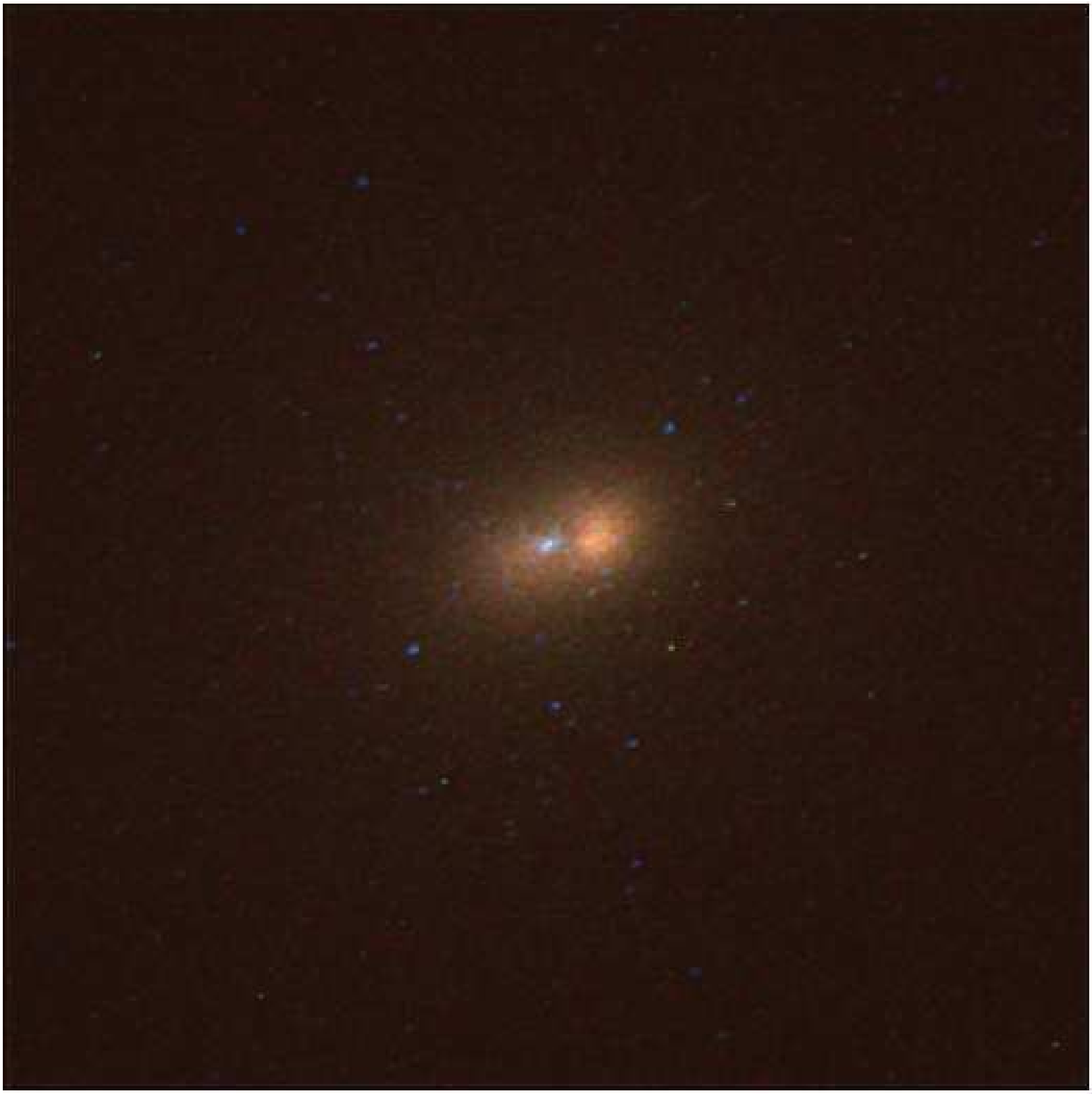

FIG. 7.– *HST* WFPC2 color image of M 31 constructed from I-, V- and 3000 Å-band, PSF-deconvolved images obtained by Lauer *et al.* (1998). The left brightness peak (with embedded blue star cluster) is P2; the right peak is P1. The I- and V-band images were substepped by half of a PC pixel, so the scale is $0\farcs0228$ pixel^{-1}. The 3000 Å image was not substepped; we matched it to the I- and V-band images by interpolation.

It should be noted that Tremaine fitted his model only to the WFPC1 photometry. The resulting (reasonably good) match to kinematic measurements with $\sigma_* = 0\farcs5$ was a test of the model and not a feature built into it. That test was encouragingly successful, but small discrepancies already implied that a better model might result from a fit to both the photometry and the kinematics. Now the kinematic resolution has improved by a factor of two. It would be no surprise if the model needed further tweaking. Also, Tremaine assumed a larger ratio of BH mass to mass in stars than we do. Finally, for projection and PSF-convolution, Tremaine calculated luminosity-weighted mean V and σ moments; these are not precisely what FQ measures when it is fed a kinematically composite spectrum. Therefore, we do not expect perfect agreement with the data. For the model to successfully pass our tests, it needs only to agree with the data qualitatively well enough to support the underlying idea and quantitatively well enough to imply that tweaking would fix the fit.

We need to measure displacements of $\lesssim 0\farcs1$ with ground-based data, so we illustrate the accuracy that we can achieve by expanding the central data from Figure 4 in Figure 8. When comparing Figure 8 with displacements quoted below, note that image centroids were calculated with more pixels than are illustrated in the cuts.

6.1 Displacement of the Velocity Center From P2 Toward P1

Tremaine predicts that the velocity center of the nucleus is displaced by $0\farcs2$ from P2 toward P1. The apparent displacement is essentially the same at perfect resolution and at resolution $\sigma_* = 0\farcs52$; slit width = $0\farcs5$ (see his Fig. 3). Our resolution ($\sigma_* = 0\farcs27$; slit width = $0\farcs35$) is intermediate, so resolution is not an issue for this test.

What is important is the accuracy to which the $V = 0$ km s^{-1} point can be determined from the rotation curve. *HST* observations by themselves are not very suitable. They have superb resolution, but unless they reach well out into the bulge ($r \gg 4''$), they cannot be used to determine the velocity center by symmetrizing the rotation curve, because the rotation curve of the nucleus may be asymmetric. On the other hand, we have measured $V(r)$ from $-47''$ to $+36''$, so we have excellent overlap of the left and right sides of the bulge rotation curve. We can therefore subtract an accurate systemic velocity, i.e., the velocity that symmetrizes the bulge rotation curve. The zeropoint that was subtracted from the velocities in Fig. 4 and 8 is accurate to < 1 km s^{-1}. Since the rotation curve is very steep near the center, the place where $V = 0$ km s^{-1} is determined to $\pm 0\farcs010$. The velocity center is assigned radius $r = 0''$ in Tables 2 and 3 and in Figures 4 and 8.

We find that the velocity zero radius is displaced from the UV cluster in the P1 direction by $0\farcs051 \pm 0\farcs014$. With respect to the center of P2 (not including light from the UV cluster), the velocity center is displaced toward P1 by $0\farcs080 \pm 0\farcs011$. After bulge subtraction, the offsets are slightly larger, $0\farcs069 \pm 0\farcs014$ and $0\farcs098 \pm 0\farcs011$, respectively. These are smaller than the offset predicted by Tremaine, but they are in the expected direction.

6.2 Asymmetry in the Rotation Curve

A necessary consequence of Tremaine's model is that the rotation curve is asymmetric. The apparent asymmetry depends on resolution. At $\sigma_* = 0\farcs52$, it is small. At $\sigma_* = 0\farcs37$ and slit width = $0\farcs5$ (Bacon *et al.* 1994), the maximum rotation velocity $V_{\rm max}$ is ~ 10 km s^{-1} higher on the P2 side than on the P1 side. At perfect resolution, the asymmetry in $V_{\rm max}$ is ~ 60 km s^{-1}. Also, at perfect resolution, $V_{\rm max}$ is reached at $r = -0\farcs3$ on the P2 side but at $r = +0\farcs7$ on the P1 side. These predictions are for the total, not the bulge-subtracted, spectrum.

Before bulge subtraction, we observe a slight asymmetry in the sense predicted: $V_{\rm max} = -159 \pm 3$ km s^{-1} on the P2 side and $+152 \pm 2$ km s^{-1} on the P1 side. The difference in $|r|(V_{\rm max})$ is not significant. After bulge subtraction, the asymmetry in the nucleus is much more pronounced: $V_{\rm max} = -233 \pm 4$ km s^{-1} at $r = -0\farcs68 \pm 0\farcs03$ on the P2 side and 179 ± 2 km s^{-1} at $r = 0\farcs86 \pm 0\farcs1$ on the P1 side. The difference in $|r|(V_{\rm max})$ is small, but the difference in rotation amplitude is not: $\Delta V_{\rm max} = 54 \pm 4$ km s^{-1}. More than any other observation in this paper, we regard this as strong support for the essential idea that stellar orbits are eccentric and coherently aligned.

6.3 Velocity Dispersion of P1

Tremaine also predicts that P1 is colder than the bulge. At infinite resolution, the model's minimum dispersion is $\sigma \simeq 135$ km s^{-1} at $r = 0\farcs6$. We observe a smaller minimum $\sigma = 123 \pm 2$ km s^{-1} at a larger radius, $r \simeq 0\farcs92$. But P1 is clearly colder than the bulge; the bulge dispersion decreases inward from 160 ± 1 km s^{-1} at $r \geq 25''$ to 145 ± 1 km s^{-1} at $4'' \leq r \leq 8''$ (all errors are internal).

Bulge subtraction shows that the nucleus has $\sigma \lesssim 100$ km s^{-1} at $|r| \gtrsim 1''$ on both sides of the center. In the context of Tremaine's model, the natural interpretation is that many eccentric orbits have escaped from the alignment with P1 and are phase-mixed around the center.

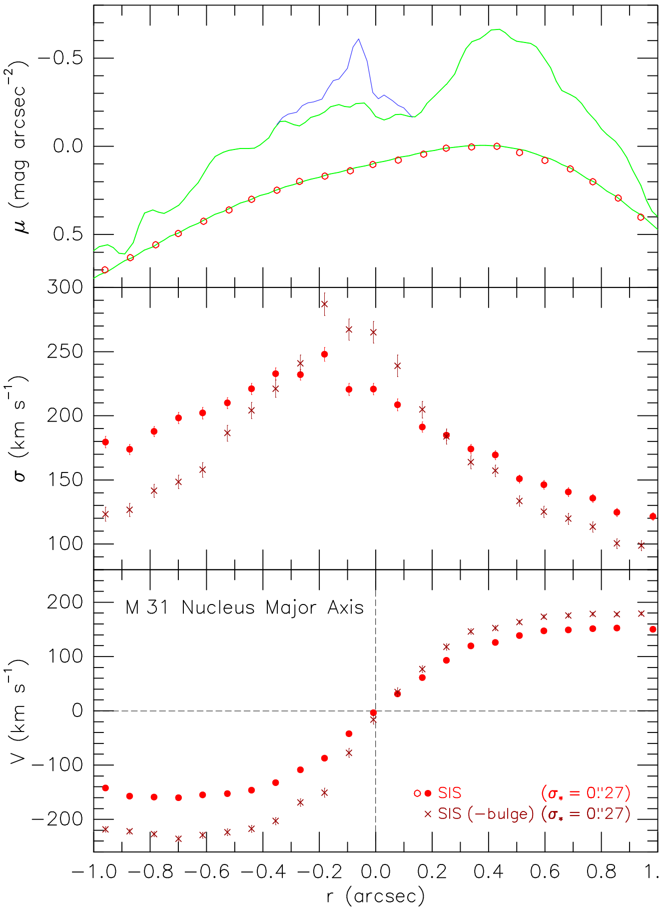

FIG. 8.– Rotation velocity, velocity dispersion, and surface brightness cuts along the major axis of the nucleus of M 31. The lines and symbols have the same meaning as if Figure 4.

6.4 The Velocity Dispersion Peak at P2

In agreement with our observations, the model has a much steeper dispersion gradient on the P1 side than on the P2 side. It predicts a maximum dispersion of $\sim$ 300 km s^{-1} at perfect resolution or $\sim$ 242 km s^{-1} at resolution $\sigma_* = 0\farcs37$; slit width = $0\farcs5$. This agrees adequately with our observation of 248$\pm$5 km s^{-1} at $0\farcs27$ resolution. In any case, the model's maximum dispersion is easily changed by adjusting the BH mass or the disk density near the center.

6.5 Conclusion

We conclude that Tremaine's nuclear disk model passes our tests, at least qualitatively. Its main shortcoming is that it assumes that all of the nuclear orbits are aligned. The observations show that some of the nucleus is not part of the P1 – P2 alignment; we interpret this to mean that some eccentric orbits have phase-mixed around the center. Tweaking seems required. Better agreement with the low observed velocity dispersion might be obtained by making the eccentric orbits more elongated and by pointing them more nearly at us. But as a proof of concept, the model works remarkably well. If the nucleus is in equilibrium, then our detection of asymmetry in the rotation curve and in the h_3 profile is essential confirmation of the idea that many of the stars revolve around the BH in eccentric and aligned orbits.

If P1 and P2 are part of the same eccentric disk, then their stellar populations should be very similar. P1 stars contribute to P2 when they are near pericenter. P2 also contains stars that never reach P1, and the nucleus may have a radial gradient in properties. But the differences between P1 and P2 are not likely to be large. This final test of Tremaine's model is carried out in the next section.

7. STELLAR POPULATIONS IN THE NUCLEUS

Figures 9 and 10 summarize our observations of the stellar populations of P1, P2, and the inner bulge of M 31. Figure 9 shows the equivalent widths (EW) of the Mg triplet (Mg$_b$), four Fe lines, the Ca infrared triplet, and Hβ as a function of radius. The EWs were derived using the Lick system of continuum and line windows (Faber *et al.* 1985), except for the Ca triplet lines, for which we used the window definitions of Díaz, Terlevich & Terlevich (1989). The indices were corrected for velocity dispersion broadening; they refer to a standard dispersion of 220 km s^{-1} (instrumental plus kinematic broadening), in accordance with the Lick system. For better S/N, we averaged the EWs of the three Ca triplet lines and the EWs of the four FeI lines (λ = 5015 Å, 5270 Å, 5335 Å, 5406 Å). The averaged indices are denoted <Ca>$_3$ and <Fe>$_4$. In Figure 10, we also show parts of the spectra of P1, P2 and the inner bulge of M 31, and we compare P1 with M 32 and with the kinematic template stars. Before overplotting, the spectra were redshifted and broadened to match LOSVDs. Also, the continua were removed with low-order polynomials.

In the Mg region, the stellar populations of P1, P2, and the bulge are extremely similar. Differences in the Mg$_b$ indices are $\lesssim$ 5 % (Fig. 9). The nucleus has slightly stronger Ca lines than the bulge. However, within the errors, P1 and P2 have the same Ca EWs.

Figures 9 and 10 clearly show that M 31 and M 32 are different, both in absolute and in relative line strengths. Strong Hβ and weak Mg$_b$ absorption could in part be a sign that M 32 is younger than M 31 (e. g., Faber *et al.* 1995; see Freedman 1992 and Davies 1996 for reviews). An older version of M 32 might be more like M 31 in Hβ and overall metal line strengths, but it is not likely to account for the difference between Mg$_b$ and <Fe>$_4$. Relative to iron, M 31 has a Mg overabundance similar to that in bright ellipticals (e. g., Worthey *et al.* 1992). In contrast, M 32 is consistent with solar [Mg/Fe] values. Therefore it is unlikely that P1 could be the almost-digested remnant of an elliptical like M 32. It is also unlikely that P1 is made of globular cluster stars, because no known globular has the required high metal line strengths, either in our Galaxy or in M 31 (e. g., Burstein *et al.* 1984).

Figure 10 also compares P1 with the standard stars used as kinematic templates. In the Ca triplet region, K0 III stars (especially η Cyg) give marginally the best fit, but others were used as well and gave similar results. The M3 III star 3 Aqr is almost as good as η Cyg. Clearly this wavelength region is very insensitive to stellar population differences. This is precisely why it is so well suited to kinematic measurements (Dressler 1984). In the Mg triplet region, no single star gives a satisfactory match to M 31, but a combination of a G8 V star and a K2 III star gives an excellent fit.

Figures 9 and 10 imply that *P1 is more similar to P2 than either is similar to the bulge or to any globular cluster.* This is consistent with Tremaine's model.

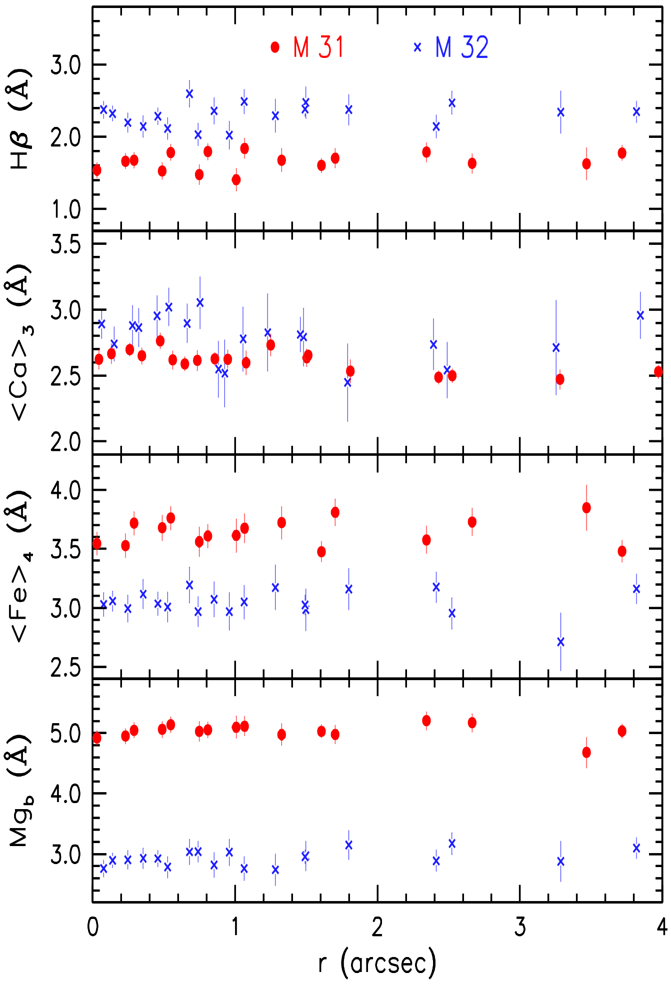

FIG. 9.– Absorption line strengths in M 31 (filled circles) and M 32 (crosses). The line indices are defined in the text.

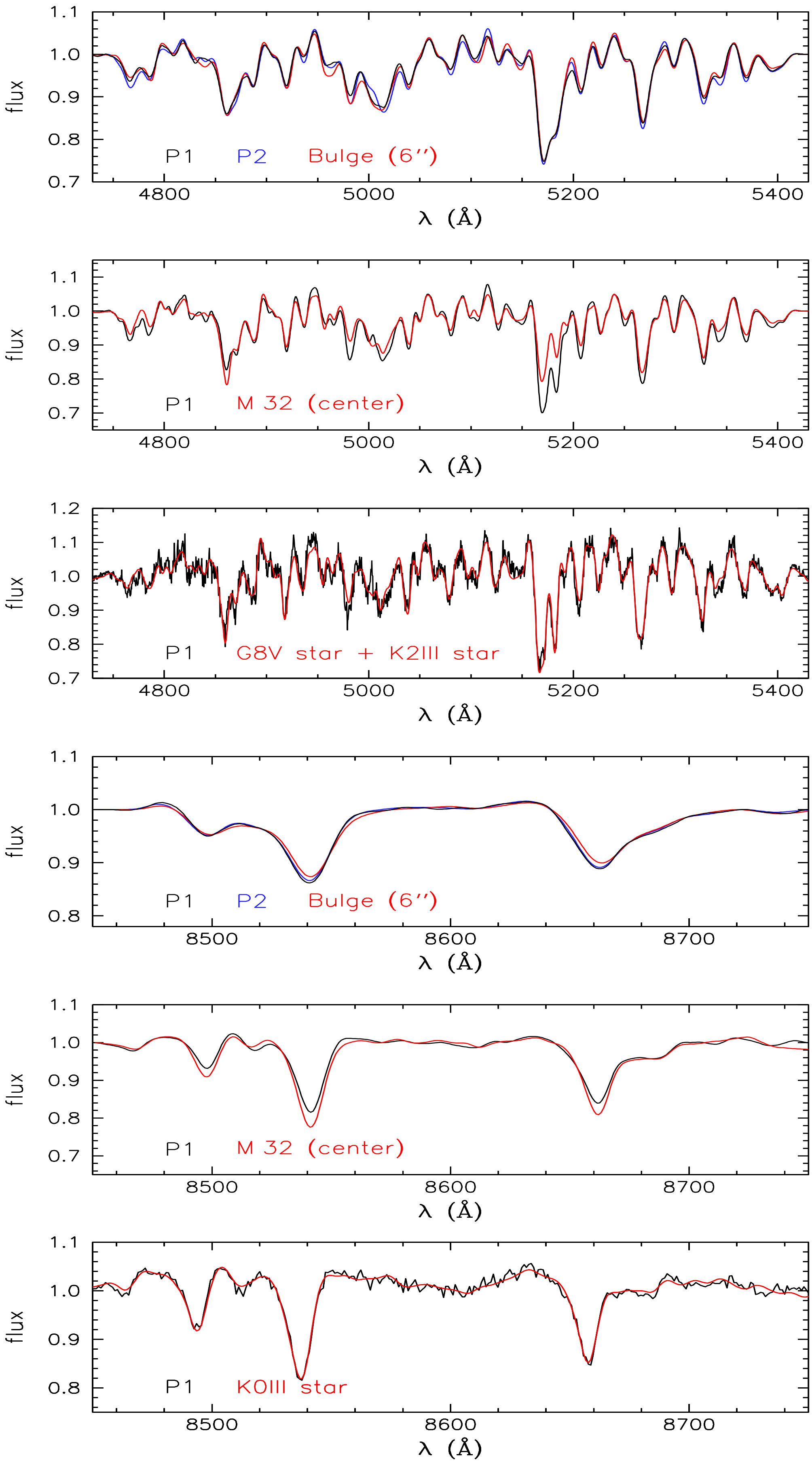

FIG. 10.– Comparisons between the spectra of P1, P2, and the bulge of M 31, and between the spectra of P1, the center of M 32, and the template stars used for the kinematic analysis.

8. LOCATING THE BLACK HOLE VIA THE POSITION OF THE CENTER OF MASS

In this section, we combine the SIS spectroscopy with the WFPC2 images and reexamine the case for a BH in M 31. We show that we can locate the BH with some confidence, and we argue that it is offset by $0''.07 \pm 0''.01$ from the center of the galaxy. This result provides a constraint on the BH mass. We also suggest that any dark cluster alternative to a BH must be $\lesssim 0''.13$ in radius. As a result, the BH detection becomes stronger: the mass-to-light ratio at $r \leq 0''.13$ is $M/L_V \simeq 300$ (§ 9).

We suggest that the BH is located in the UV star cluster embedded in P2. Initial motivation is provided by the dynamical prediction (Tremaine 1995) that the *true* velocity dispersion peak is very close to the BH. Also, Tremaine predicts and we observe that the dispersion gradient is shallower on the P2 side than on the P1 side. Therefore, PSF convolution moves the *apparent* dispersion peak away from the true peak in the anti-P1 direction. This effect is more general than Tremaine's model; it follows from any such asymmetry, no matter what the cause. The peak in the bulge+disk dispersion profile is located $0''.18$ – $0''.23$ from the velocity center in the anti-P1 direction (§ 6; Fig. 8). Therefore it is $0''.13$ – $0''.18$ away from the UV cluster in the anti-P1 direction. Tremaine predicts that the apparent dispersion peak is $0''.1$ – $0''.2$ away from the BH in the anti-P1 direction (see his Fig. 3). This implies that the BH is close to the UV cluster. Furthermore, after bulge subtraction, the dispersion profile is more symmetrical, so the apparent dispersion peak is moved less by PSF convolution. Figure 8 shows that the three highest-σ points are the ones closest to the UV cluster. It is remarkable that the σ profile is so peaked (the highest-σ data points span $0''.17$, but the PSF has a FWHM of $0''.64$). Finally, the UV cluster identifies a special place in P2, and there are reasons to expect UV-bright stars near a BH. All of these arguments point to the UV cluster as the location of the BH. Nevertheless, we would not make this suggestion if we did not have a further dynamical argument to support it. We turn to this argument next; it is illustrated in Figures 11 and 12.

We assume that the central part of M 31 is in dynamical equilibrium. I. e., we assume that the center of mass of the combined nucleus and BH is at the center of the bulge. We measure the position of the center of the bulge using H- and K'-band images from Wainscoat & Kormendy (1998). We find the position of the rotation center. The center of mass of the nucleus and BH can be found if we add $L/M \times 3.3 \times 10^7$ M$_\odot$ to the WFPC2 image at the position of the BH and calculate the first moment of the resulting light distribution. If we have correctly located the BH, then these three positions should agree.

Figure 12 compares the positions of the blue cluster, P1, P2, the velocity center, the center of mass, and the center of the bulge. Coordinates X and Y are measured parallel and perpendicular to our slit orientation, which is approximately the major axis of the nucleus. The origin, $(X, Y) = (0, 0)$, is the center of the bulge, determined as follows. Isophote fitting of a variety of images was carried out using procedures described in Bender & Möllenhoff (1987) and in Bender, Döbereiner, & Möllenhoff (1988). These provide isophote center coordinates $X_{\rm center}$ and $Y_{\rm center}$ as a function of isophote major axis radius a. We found that the center of the bulge cannot reliably be determined from V- and I-band images because of dust absorption (McElroy 1983; Wainscoat & Kormendy 1998). Instead, we measured center coordinates on H and K' images obtained by Wainscoat & Kormendy (1998) using two infrared cameras on the University of Hawaii 2.2 m telescope. The NICMOS-3 camera uses a 256 × 256 pixel HgCdTe array with scale $0''.124$ pixel^{-1} (Hodapp *et al.* 1992); QUIRC is a 1024 × 1024 pixel HgCdTe camera with scale $0''.06$ pixel^{-1} (Hodapp *et al.* 1996). The infrared images show strong surface brightness fluctuations due to the finite numbers of stars that contribute significant light to each PSF area (Tonry & Schneider 1988). However, dust is not an issue at these wavelengths. Plotting X and Y against a reveals an unexpected result: *The positions of the centers of bulge isophotes oscillate with isophote radius by* $\pm 0''.1$ *in* X *and almost* $\pm 0''.2$ *in* Y. This is not produced by the surface brightness fluctuations. Results from QUIRC and NICMOS-3 agree reasonably well, and results in H and K' agree very well. The variations in Y are large and poorly sampled, so we cannot derive the Y center position reliably. However, the X center, which is the important one for the BH case, is well determined ($\pm 0''.011$ error bar in Fig. 12).

At $r < 1''$, the center coordinates determined from the infrared images locate P1 with good precision. The QUIRC camera was used with the tip-tilt secondary mirror of the 2.2 m telescope; the images have resolution $\sigma_* = 0''.092$ to $0''.097$. The infrared images therefore provide a substantial radius range, $0''.7$ – $2''$, where $X_{\rm center}$ can be normalized to the measurements of the *HST* images.

To determine center coordinates of different parts of the nucleus, we used the deconvolved V-band *HST* image. This shows the UV cluster well enough to locate its center via the position of the brightest pixels in P2 (blue filled circle in Fig. 12; white dot in Fig. 11 – see below). Also, the I-band image is more affected by surface brightness fluctuations; since there are relatively few pixels per isophote, these introduce significant noise. We measured the V-band image twice, once with the region around P2 masked off to determine the position of P1 (green line), and once with P1 masked off to measure P2 (blue line). In the latter case, the center coordinates at $a^{1/4} \simeq 0.6$ – 0.7 are those of P2 as a whole; at smaller radii, the center moves $0''.03$ toward positive X as it becomes dominated by the UV cluster.

The position of the velocity center requires discussion. Figure 12 shows the X coordinate of the *apparent* velocity center, determined earlier to $\pm 0''.010$. However, Statler (1998), Tremaine (1998), and the referee emphasize that the rotation curve of the nucleus should cross the systemic velocity at a position different from the center of mass. The size of the offset depends on the amount of asymmetry in the rotation curve that is produced by the eccentric orbits. We believe that we have detected the asymmetry, but it is large only in the bulge-subtracted spectrum. The rotation curve of the bulge plus nucleus is symmetric enough and steep enough near the center so the offset should not be large. Also, to the extent that the rotation curve is symmetric, PSF convolution does not move it. However, we do not know the intrinsic (pre-PSF) rotation curve, so we cannot easily estimate the offset. Therefore we also located the center of the bulge rotation curve and separately that of the outer rotation curve ($r \geq 2''$) of the nucleus. Here Tremaine's model predicts little rotation asymmetry. All three rotation symmetry points are mutually consistent. The apparent rotation center is at $X = -0''.017 \pm 0''.010$ with respect to the bulge center (Fig. 12). The rotation curve of the nucleus at $r \geq 2''$ is symmetric about $X = -0''.007 \pm 0''.060$. The zero velocity position of the bulge rotation curve at $-10'' \leq r \leq -5''$ and at $+5'' \leq r \leq +12''$ is at $X = -0''.025 \pm 0''.25$. The

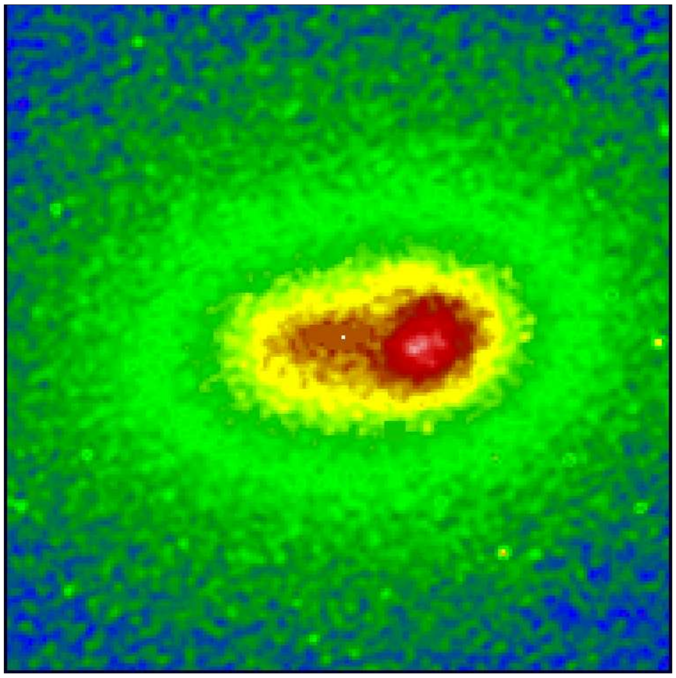

FIG. 11.– *HST* WFPC2 *V*-band image of M 31. The SIS slit is nearly horizontal. The surface brightness contributed by the UV cluster has been clipped out; these stars are assumed to have small mass-to-light ratios. The white dot indicates the BH: the intensity added is 3.3×10^7 $M_\odot$ divided by the mass-to-light ratio of the stars, $M/L_V \simeq 5.7$ (Kormendy 1988b), converted to an apparent magnitude and thence to ADU. The area shown is 186 pixels = 4$''$.24 square. The center of mass of the combined BH and nucleus is found by calculating the luminosity centroid of this image.

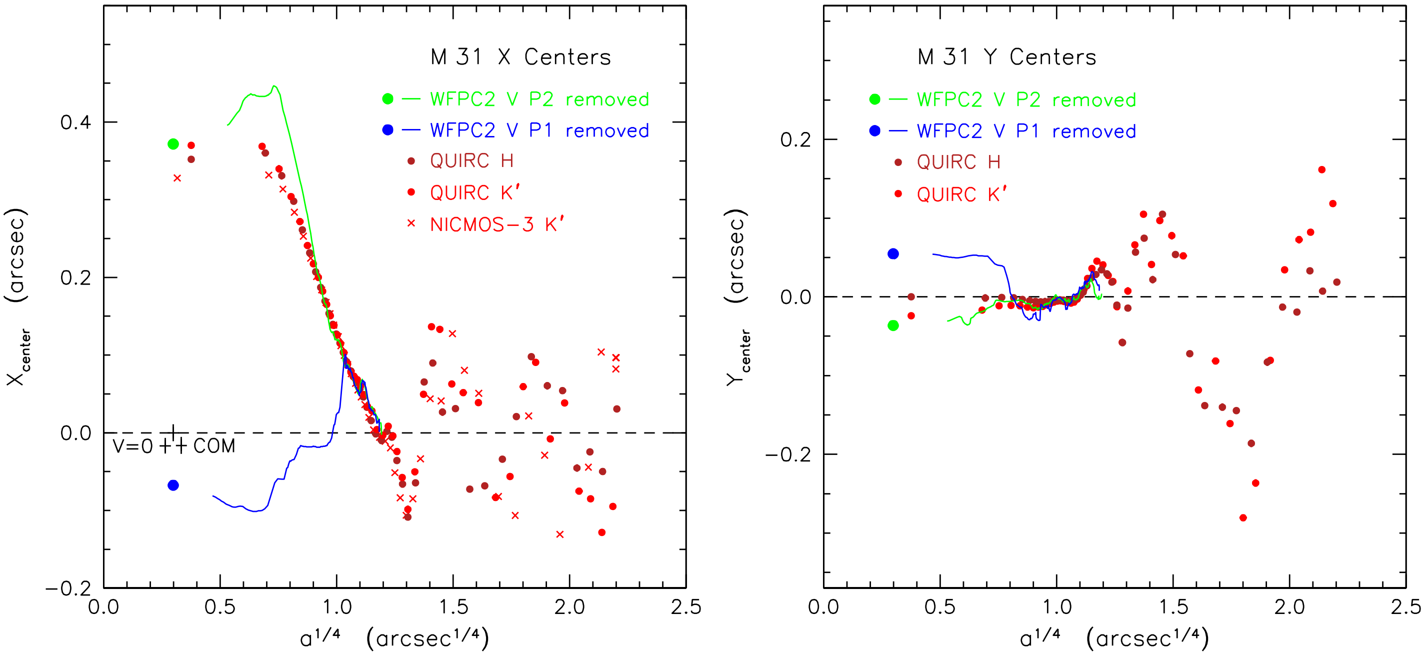

FIG. 12.– (*left*) Isophote center *X* coordinate (almost horizontal in Fig. 11) as a function of isophote major-axis radius *a*. The *V*-band WFPC2 image (cf. Fig. 11, but including the UV cluster and not the artificial BH) was measured twice, once masking out the regions dominated by P2 (green) and once masking out P1 (blue). The green and blue dots show the positions of the centers of P1 and the UV cluster, respectively. The brown and red points are measurements of individual isophotes in *H*- and *K'*-band images from Wainscoat & Kormendy (1998). All of the *X(a)* measurements have been normalized to agree at 1$''$.1 – 2$''$. (*right*) Corresponding isophote *Y* coordinates (almost vertical in Fig. 11) as functions of isophote radius *a*. In both panels, $X = 0$ and $Y = 0$ are at the center of the bulge; the associated error bar is indicated in the left panel. The positions of the velocity center and of the center of mass of the bulge and nucleus, each with error bars, are shown by the symbols labeled "V=0" and "COM". They are plotted at arbitrary *a*. The photometry procedure is from Bender & Möllenhoff (1987) and from Bender *et al.* (1988).

agreement may be fortuitously good, but it suggests that the apparent $V = 0$ position is close to the true velocity center. Nevertheless, given the uncertainties, we base our argument mainly on the position of the bulge center.

Finally, the point labeled "COM" shows the position of the center of mass. To locate it, we assumed that the BH has mass $M_\bullet = 3.3 \times 10^7$ M$_\odot$ (Dressler & Richstone 1988; Kormendy 1988b, see Kormendy & Richstone 1995) and that the stars in the nucleus have $M/L_V = 5.7$ (the value found in Kormendy 1988b for the above BH mass, corrected for a distance of 770 kpc). We added $3.3/5.7 \times 10^7$ $L_{V\odot}$ of luminosity to the deconvolved V-band WFPC2 image at the position of the brightest pixel in the UV cluster. We had previously clipped out the excess brightness contributed by the UV cluster, on the grounds that these stars probably have small mass-to-light ratios. Actually, very little light was removed. The resulting image is shown in Fig. 11. A centroiding algorithm written to run under the image processing system *MIDAS* was then used to find the luminosity-weighted center coordinates. We adopted results for a $3\farcs5 \times 3\farcs5$ region centered iteratively at the COM, but we checked that the results are insensitive to the size of the box used. The error bar shown in Fig. 12, $\pm0\farcs011$, reflects the differences in results obtained for different box centers.

The center of mass of the nucleus plus BH and the velocity center agree with each other and are at the center of the bulge to within the errors of measurement. This is the dynamical argument that the BH is in the UV cluster.

The agreement of the COM with the bulge center confirms the dynamical model measurements of $M_\bullet$ and M/L_V using a new technique. It increases our confidence in the results, because the coupling between $M_\bullet$ and M/L_V is opposite to what it is when we model kinematic data. Model $M_\bullet$ and M/L_V values are inversely coupled: we can preserve a good fit to V and σ by (e. g.) decreasing $M_\bullet$ and increasing M/L_V such that the total mass near the center remains constant. Here, to preserve the agreement of the COM with the rotation and bulge centers, we must raise or lower $M_\bullet$ and M/L_V together.

We apply this argument to constrain $M_\bullet$ as follows. We use an approximate version of the dynamical modeling results – it is beyond the scope of this paper to calculate new models to explore the diagonal valley in χ^2 space that comes from the $M_\bullet$ – M/L_V coupling. Instead, we vary $M_\bullet$ and M/L_V together, keeping constant the total mass inside $r = 1''$. The choice of this radius is subjective, but it is approximately the radius of gravitational influence of the BH, and it is approximately the radius at which the apparent rotation curve peaks. We aim to preserve $V(1'')$. Choosing a smaller radius would make the error bars smaller; a larger radius seems inappropriate because it would include stars that do not much feel the BH. For $M/L_V = 5.73$, the mass in stars in a sphere of radius $1''$ is $M_* \sim 1.7 \times 10^7$ M$_\odot$. The total mass inside $1''$ is $M_\bullet + M_* \simeq 5.0 \times 10^7$ M$_\odot$. We then vary $M_\bullet$ and M/L_V together and calculate the position of the COM.

We find that small $M_\bullet$ values are weakly constrained: if $M_\bullet \leq 1.5 \times 10^7$ M$_\odot$, then the COM is $\geq 0\farcs033 \pm 0\farcs02$ on the P1 side of the bulge center. A stronger constraint comes from the mass-to-light ratios: $M/L_V \simeq 12$ to 17 is implausibly large for an old stellar population in a small bulge (Bender, Burstein & Faber 1992). This is the essence of the dynamical model results: more strongly than the COM argument, they show that the kinematics imply too much mass in stars unless there is a central dark object. They also show that the dark mass must have a small radius to explain the V and σ gradients near the center.

High $M_\bullet$ values are strongly constrained by the COM argument. We find that BH masses larger than about 4×10^7 M$_\odot$ put the COM too close to the UV cluster, where it is no longer consistent with the bulge center. The maximum BH mass allowed by the total mass constraint is 5×10^7 M$_\odot$, considerably smaller than the largest values quoted in the literature. Before $M_\bullet$ reaches this value, M/L_V for the stars becomes implausible small.

We conclude that 1.5×10^7 M$_\odot \lesssim M_\bullet \lesssim 4.5 \times 10^7$ M$_\odot$ if $M/L_V \simeq 5.73$. Remarkably, $M_\bullet = 3.3 \times 10^7$ M$_\odot$ results in excellent agreement between the COM and velocity center. The $M_\bullet$ range that is allowed by the COM argument is $\propto M/L_V$. Small masses are supported by several authors: $M/L_V = 4.5 \pm 0.4$ (Kent 1989); $M/L_V \sim 4.5$ (Bacon *et al.* 1994; both values are for $D = 770$ kpc). Some models in Kormendy (1988b) had slightly higher $M_\bullet$ and M/L_V values. Dressler & Richstone (1988) get approximately the same ratio of BH mass to mass in stars as we have found but $M_\bullet$ and M/L values that are higher by a factor of ~ 2. However, what is not allowed by the COM argument is the combination of high $M_\bullet$ and small M/L_V.

This result is a concern for the Tremaine (1995) model, because the mass of stars at $r \leq 1''$ is not small compared to the BH mass. The stars add up to about half of $M_\bullet$. Tremaine adopted a high $M_\bullet = 7.5 \times 10^7$ M$_\odot$ and a small $M/L_V = 4$. These assumptions put the COM very close to the BH, $0\farcs052 \pm 0\farcs014$ on the P2 side of the bulge center.

It is not easy to escape this conclusion without violating the assumptions. If we make $M_\bullet/M_*$ larger, then we can save the COM argument only by putting the BH closer to the bulge center. But then it would be near the "surface" of the UV cluster (see Fig. 8). This is an essentially massless clump of stars centered where the circular orbital period around the BH is ~ 1000 yr. BH tides would shear the cluster and phase mix it away in a few hundred years. This is another reason why we suggest that the BH is at the center of the UV cluster.

The COM argument is vulnerable for at least two reasons. First, the procedure that we used is somewhat model dependent. For example, if we traded BH mass against the stellar mass inside a different radius, we would get slightly different $M_\bullet$ limits. Also, the assumption of equilibrium – the assumption that the COM is at the center of the bulge – may be wrong if the oscillation in isophote center coordinates is a sign of oscillation in the mass distribution. However, our argument is not dependent on the resolution of the ground-based spectroscopy: the COM position is determined only from the *HST* WFPC2 image and an assumed BH mass. Also, it is compelling to find such good agreement between the bulge center, the velocity center (found in three different ways), and the COM determined by using the BH mass from the dynamical modeling papers.

Finally, we note that the consistency of the COM with the (velocity and) bulge centers constitutes the detection of an offset of the BH from the galaxy center that balances the photometric asymmetry. Far from being a worrying sign of non-equilibrium dynamics, the kinematic asymmetry mapped by Bacon *et al.* (1994) and seen at higher resolution in Figures 4 and 8 becomes a necessary consequence of dynamical equilibrium.

9. IMPROVED CASE FOR A MASSIVE DARK OBJECT IN M 31

The results of §§ 6 – 8 also strengthen the case for a massive dark object in M 31. To the extent that our observations support Tremaine's eccentric disk model, they also imply a maximum possible radius for any dark cluster alternative to a BH. Maintaining the coherent alignment of the elongated orbits is difficult at best because the contribution of the stars to the potential is not negligible. But it is impossible on time scales much longer than one orbital time unless the massive dark object (MDO) looks like a central point mass to the orbits. In practice, this means that it must be smaller than their pericenter radii. Estimating this limit is nontrivial, because the model has not been optimized for the present data. As noted in § 6, the observations suggest that the orbits are more elongated than Tremaine assumed. A reasonable estimate can be derived from Figure 8, which shows that the highest-σ point is displaced from the UV cluser by $0\farcs13 \pm 0\farcs03$. In the model, the highest dispersion point is aproximately where the stars turn around at pericenter. We conclude that any MDO cluster has radius $r_{\rm MDO} \lesssim 0\farcs13$. This constraint implies a higher central mass-to-light ratio than the maximum values derived in previous studies.

At $r \leq 0\farcs13$, the projected V-band light is 16.9 mag, corresponding to $M_V = -7.8$ or 110,000 $L_{V\odot}$. The mass of these stars is negligible for any plausible mass-to-light ratio. Adopting $M_\bullet = 3.3 \times 10^7$ $M_\odot$ from the COM and dynamical studies, the projected mass-to-light ratio inside $r = 0\farcs13$ is

$$\frac{M}{L_V} = 300 \left(\frac{M}{L_V}\right)_\odot . \qquad (5)$$

If the central dark object is spherical, then we can use the deprojected brightness profile of P2 plus the bulge (P1 is too far away to matter) to derive the mass-to-light ratio inside a sphere or radius $0\farcs13$. We obtain

$$\frac{M}{L_V}\left(\text{sphere of radius } 0\farcs13\right) \simeq 2{,}200 \left(\frac{M}{L_V}\right)_\odot . \qquad (6)$$

Even if the dark object is not spherical, the mass-to-light ratio inside the smallest sphere that contains it is not likely to be more than 2 – 4 times smaller.

These mass-to-light ratios are significantly larger than the maximum values derived by Dressler & Richstone (1988), Kormendy (1988b), and Bacon *et al.* (1994). Therefore the combination of the COM argument and the support of the observations for Tremaine's model has strengthened the case for an MDO in M 31.

The arguments that the MDO is a BH remain indirect. Our limit, $r_{\rm MDO} \lesssim 0\farcs13$ is a factor of $\sim$4 better than previous limits based on the spatial resolution of kinematic measurements. This is a factor of 2 too large to provide a rigorous case against dark clusters made of stellar remnants and substellar objects. Goodman & Lee (1989) argued that such a cluster would be ruled out in M 31 if its half-mass radius were $r_h < 0\farcs1$. Richstone *et al.* (1990) made a similar point. Maoz (1995, 1998) has calculated maximum MDO lifetimes against evaporation of high-mass remnants and collisions of substellar objects. If we assume conservatively that the MDO cluster is a Plummer model with 75 % of its mass inside $r_{\rm MDO}$, then the half-mass density is $\rho_h \simeq 1.6 \times 10^8$ $M_\odot$ pc^{-3}. For a half mass of $M_h = 1.65 \times 10^7$ $M_\odot$, the maximum MDO lifetime is 1×10^{11} yr, similar to that in M 32 (see Maoz 1998, Fig. 1). Astrophysical arguments against BH alternatives remain strongest in the Galaxy and in NGC 4258 (Maoz 1995, 1998; Genzel *et al.* 1997).

10. CONCLUSION

We concluded in § 8 that we have detected the offset of the BH from the dynamical center of M 31. Since we already knew that the starlight is asymmetric, an offset was expected (Tremaine 1995). Detecting it has provided a new way to measure the relative mass of the BH and the stars using the location of their combined center of mass. We argued that the BH is in the UV star cluster; this also improves the limit on the size of the dark object to $r_\bullet \lesssim 0\farcs13 \pm 0\farcs03$. This implies a large maximum mass-to-light ratio, $M/L_V(r \leq 0\farcs13) = 300$ (projected) or 2,200 (unprojected). The BH detection is strengthened.

As discussed in §§ 6 and 7, our observations support Tremaine's (1995) model that both nuclei of M 31 are part of the same eccentric disk of stars orbiting the BH. In particular, we regard the detection of asymmetry in the nuclear rotation curve as essential confirmation that stellar orbits are eccentric and coherently aligned. However, we find that the nuclear velocity dispersion at $r \gtrsim 1''$ is small ($\sigma \lesssim 100$ km s^{-1}) on both sides of the center. We interpret this to mean that many of the eccentric orbits have escaped from the P1 – P2 alignment and phase-mixed around the center. Since the mass in stars inside $1''$ is not small compared to $M_\bullet$, it seems reasonable to further conclude that maintaining the alignment is getting more difficult and that the decay of the double nucleus is accelerating.

We do not know whether the double nucleus is the cause or an effect of the offcenter BH. However, offcenter BHs are an inevitable consequence of hierarchical structure formation and galaxy merging (Begelman, Blandford, & Rees 1980). If most large galaxies contain BHs, then galaxy mergers produce binary BHs and, in three-body encounters, BH ejections with recoil (see Valtonen 1996 for a review). How much offset we see, and indeed whether we see two BHs or one or none at all, depend on the relative rates of mergers, dynamical friction, and binary orbit decay (Xu & Ostriker 1994). Offcenter BHs may have much to tell us about these and other processes (see Tremaine 1997 and Faber *et al.* 1997 for reviews). The observation of central asymmetries in a significant fraction of galaxies surveyed (Lauer *et al.* 1995) and the detection in NGC 4486B of a second double nucleus (Lauer *et al.* 1996) containing a BH (Kormendy *et al.* 1997) suggests that a search for offcenter BHs and active galactic nuclei may be a profitable subject for further study.

We thank Olivier Le Fèvre and Christian Vanderriest for their support of the observing runs. We also thank Neil Trentham for his assistance during the observations. Accurate location of the bulge center would have been impossible without infrared photometry; we are grateful to Richard Wainscoat for letting us use results from Wainscoat & Kormendy (1998) before publication. It is a pleasure to thank Josh Barnes and Scott Tremaine for helpful conversations. We particularly thank Scott Tremaine and the referee, Tom Statler, for pointing out an important mistake in the first version of the paper. Tom Statler's careful reading was extremely helpful and resulted in important improvements to the paper. JK is grateful to the Alexander von Humboldt-Stiftung (Germany) for the Research Award that made possible his visit to the Universitäts-Sternwarte, Ludwig-Maximilians-Universität, Munich. He also thanks the Sternwarte for its hospitality. JK was supported in part by NSF grant AST-9219221. JK and RB were also supported by Sonderforschungsbereich 375 of the German Science Foundation and by the Max-Planck-Gesellschaft.

REFERENCES

Andredakis, Y. C., & Sanders, R. H. 1994, MNRAS, 267, 283
Bacon, R., Emsellem, E., Monnet, G., & Nieto, J. L. 1994, A&A, 281, 691
Begelman, M. C., Blandford, R. D., & Rees, M. J. 1980, Nature, 287, 307
Bender, R. 1990, A&A, 229, 441
Bender, R. 1998, A&A, in preparation
Bender, R., Burstein, D., & Faber, S. M. 1992, ApJ, 399, 462
Bender, R., Döbereiner, S., & Möllenhoff, C. 1988, A&AS, 74, 385
Bender, R., & Möllenhoff, C. 1987, A&A, 177, 71
Bender, R., Saglia, R. P., & Gerhard, O. E. 1994, MNRAS, 269, 785
Burstein, D., & Heiles, C. 1984, ApJS, 54, 33
Burstein, D., Faber, S. M., Gaskell, C. M., Krumm, N. 1984, ApJ, 287, 586
Byun, Y.-I., *et al.* 1996, AJ, 111, 1889
Caon, N., Capaccioli, M., & D'Onofrio, M. 1993, MNRAS, 265, 1013
Crane, P. C., Dickel, J. R., Cowan, J. J. 1992, ApJ, 390, L9
Crane, P. C., Cowan, J. J., Dickel, J. R., & Roberts, D. A. 1993, ApJ, 417, L61
Davies, R. L. 1996, in Fresh Views of Elliptical Galaxies, ed. A. Buzzoni, A. Renzini, & A. Serrano (San Francisco: ASP), 175
de Vaucouleurs, G. 1948, Ann. d'Ap., 11, 267
Díaz, A. I., Terlevich, E., & Terlevich, R. 1989, MNRAS, 239, 325
Dressler, A. 1984, ApJ, 286, 97
Dressler, A., & Richstone, D. O. 1988, ApJ, 324, 701
Faber, S. M., Friel, E. D., Burstein, D., & Gaskell, C.M. 1985, ApJS, 57, 711
Faber, S. M., Trager, S. C., Gonzalez, J. J., & Worthey, G. 1995, in IAU Symposium 164, Stellar Populations, ed. P. C. van der Kruit & G. Gilmore (Dordrecht: Kluwer), 249
Faber, S. M., *et al.* 1997, AJ, 114, 1771
Freedman, W. L. 1992, in IAU Symposium 149, The Stellar Populations of Galaxies, ed. B. Barbuy & A. Renzini (Dordrecht: Kluwer), 169
Freedman, W. L., & Madore, B. F. 1990, ApJ, 365, 186
Genzel, R., Eckart, A., Ott, T., & Eisenhauer, F. 1997, MNRAS, 291, 219
Gerhard, O. E. 1993, MNRAS, 265, 213
Goodman, J., & Lee, H. M. 1989, ApJ, 337, 84
Hodapp, K.-W., Rayner, J., & Irwin, E. 1992, PASP, 104, 441
Hodapp, K.-W., *et al.* 1996, New A, 1, 177
Hoessel, J. G., & Melnick, J. 1980, A&A, 84, 317
Holland, S. 1998, AJ, 115, 1916
Jerjen, H., & Binggeli, B. 1997, in The Second Stromlo Symposium: The Nature of Elliptical Galaxies, ed. M. Arnaboldi, G. S. Da Costa, & P. Saha (San Francisco: ASP), 239
Johnson, H. M. 1961, ApJ, 133, 309
Kennicutt, R. C., *et al.* 1998, ApJ, 498, 181
Kent, S. M. 1989, AJ, 97, 1614
King, I. R., Stanford, S. A., & Crane, P. 1995, AJ, 109, 164
Kinman, T. D. 1965, ApJ, 142, 1376
Kormendy, J. 1977, ApJ, 217, 406
Kormendy, J. 1985, ApJ, 292, L9
Kormendy, J. 1987, in IAU Symposium 127, Structure and Dynamics of Elliptical Galaxies, ed. T. de Zeeuw (Dordrecht: Reidel), 17
Kormendy, J. 1988a, in Supermassive Black Holes, ed. M. Kafatos (Cambridge: Cambridge Univ. Press), 98
Kormendy, J. 1988b, ApJ, 325, 128
Kormendy, J. 1993, in IAU Symposium 153, Galactic Bulges, ed. H. Dejonghe & H. J. Habing (Dordrecht: Kluwer), 209
Kormendy, J., *et al.* 1994, in ESO/OHP Workshop on Dwarf Galaxies, ed. G. Meylan & P. Prugniel (Garching: ESO), 147
Kormendy, J., *et al.* 1997, ApJ, 482, L139
Kormendy, J., & Illingworth, G. 1982, ApJ, 256, 460
Kormendy, J., & Richstone, D. 1992, ApJ, 393, 559
Kormendy, J., & Richstone, D. 1995, ARA&A, 33, 581 (KR95)
Lauer, T. R., *et al.* 1993, AJ, 106, 1436
Lauer, T. R., *et al.* 1995, AJ, 110, 2622
Lauer, T. R., *et al.* 1996, ApJ, 471, L79
Lauer, T. R., *et al.* 1998, AJ, submitted
Light, E. S., Danielson, R. E., & Schwarzschild, M. 1974, ApJ, 194, 257
Lucy, L. B. 1974, AJ, 79, 745
Maoz, E. 1995, ApJ, 447, L91
Maoz, E. 1998, ApJ, 494, L181
McElroy, D. B. 1983, ApJ, 270, 485
Moffat, A. F. J. 1969, A&A, 3, 455
Morgan, W. W., & Keenan, P. C. 1973, ARA&A, 11, 29
Plummer, H. C. 1911, MNRAS, 71, 460
Richardson, W. H. 1972, J. Opt. Soc. America, 62, 52
Richstone, D., Bower, G., & Dressler, A. 1990, ApJ, 353, 118
Sandage, A. 1961, The Hubble Atlas of Galaxies (Washington, Carnegie Institution of Washington)
Sandage, A. 1971, in Nuclei of Galaxies, ed. D. J. K. O'Connell (Vatican City: Pontifical Academy of Sciences), 271
Sargent, W. L. W., Schechter, P. L., Boksenberg, A., & Shortridge, K. 1977, ApJ, 212, 326
Schechter, P. L., & Gunn, J. E. 1979, ApJ, 229, 472
Sérsic, J. L. 1968, Atlas de Galaxias Australes (Cordoba: Observatorio Astronomico, Universidad de Cordoba)
Stanek, K. Z., & Garnavich, P. M. 1998, ApJ, in press (astro-ph/9802121)
Statler, T. S. 1998, discussion question in Kormendy 1998, in Galaxy Dynamics, ed. D. Merritt, M. Valluri, & J. Sellwood (San Francisco: ASP), in press
Stevenson, D. J. 1991, ARA&A, 29, 163
Tody, D., *et al.* 1986, IRAF User Handbook (Tucson: National Optical Astronomy Observatories)
Tonry, J., & Schneider, D. P. 1988, AJ, 96, 807
Trager, S. C., Worthey, G., Faber, S. M., Burstein, D., & González, J. J. 1998, ApJS, 116, 1
Tremaine, S. 1995, AJ, 110, 628
Tremaine, S. 1997, in Unsolved Problems in Astrophysics, ed. J. N. Bahcall & J. P. Ostriker (Princeton: Princeton Univ. Press), 137
Tremaine, S. 1998, private communication
Tremaine, S., Ostriker, J. P. 1982, ApJ, 256, 435
Valtonen, M. J. 1996, Comments Ap., 18, 191
van den Bergh, S. 1991, PASP, 103, 1053
van der Marel, R. P. 1994, ApJ, 432, L91
van der Marel, R. P., & Franx, M. 1993, ApJ, 407, 525
Wainscoat, R. J., & Kormendy, J. 1998, AJ, in preparation
Walterbos, R. A. M., & Kennicutt, R. C. 1987, A&AS, 69, 311
Worthey, G., Faber, S. M., Gonzalez, J. J. 1992, ApJ, 398, 69
Xu, G., & Ostriker, J. P. 1994, ApJ, 437, 184